Contents lists available at ScienceDirect

International Journal of Solids and Structures

journal homepage: www.elsevier.com/locate/ijsolstr

A general framework for identification of hyper-elastic membranes with moiré techniques and multi-point simulated annealing

E. Cosola [a,b], K. Genovese [b], L. Lamberti [a,*], C. Pappalettere [a]

[a] Dipartimento di Ingegneria Meccanica e Gestionale, Politecnico di Bari, Viale Japigia 182, 70126 Bari, Italy
[b] Dipartimento di Ingegneria e Fisica dell'Ambiente, Università degli Studi della Basilicata, Viale dell'Ateneo Lucano 10, 85100 Potenza, Italy

ARTICLE INFO

ABSTRACT

This paper presents a hybrid procedure for mechanical characterization of hyper-elastic materials based on moiré, finite element analysis and global optimization. The characterization process is absolutely general because does not require any assumption on specimen geometry, loading or/and boundary conditions.

The novel experimental approach followed in this research relies on a proper combination of intrinsic moiré and projection moiré which allows 3D displacement components to be measured simultaneously and independently using always the same experimental setup and just one single camera. In order to properly compare experimental data and finite element predictions, 3D displacement information encoded in moiré patterns which are relative to the deformed configuration taken by the specimen are expressed in the reference system of the unloaded state.

A global optimization algorithm based on multi-level and multi-point simulated annealing which keeps memory of all best records generated in the optimization is used in order to find the unknown material properties through the minimization of the Ω functional built by summing over the differences between displacements measured experimentally and those predicted numerically.

Feasibility, efficiency and robustness of the proposed methodology are demonstrated for both isotropic and anisotropic specimens subject to increasing pressure loads: a natural rubber membrane and a glutaraldehyde treated bovine pericardium patch, respectively. Remarkably, the results of the characterization process are in very good agreement with target data independently determined. For the isotropic specimen, the maximum error on hyper-elastic constants is less than 1% and the residual error on displacements is less than 3.5%. For the anisotropic specimen, the maximum error on material properties is about 3.5% while the residual error on displacements is less than 3%. The identification process fails or becomes less reliable if "local" displacement values are considered.

1. Introduction

Mechanical characterization of hyper-elastic materials is nowadays a very challenging engineering problem since this class of materials is often utilized to model soft biological tissues (Fung, 1993; Ogden, 1997; Humphrey, 2003; Holzapfel, 2004). Many constitutive models are available for isotropic hyper-elastic materials and allow the characterization process to be carried out in a rather standardized manner. Hyper-elastic constants can be obtained by fitting a stress–strain curve determined experimentally. Planar biaxial testing (Sacks, 2000), where a square specimen is subject to biaxial tension,

* Corresponding author. Tel.: +39 080 5962774; fax: +39 080 5962777.
E-mail address: lamberti@poliba.it (L. Lamberti).

and inflation test (Wineman et al., 1979), where a flat circular membrane is progressively expanded by uniform pressure, are the two experimental protocols most widely utilized in the characterization of hyper-elastic materials.

However, the above-mentioned approach can yield inaccurate results when the material possesses a high degree of in-homogeneity and anisotropy or undergoes a general state of stress as it happens in the case of natural and synthetic biological tissues. Continuum mechanics theory states that, regardless of load non-uniformity, material in-homogeneity/anisotropy and type of boundary conditions, the structural response is univocally defined by the values of *u*, *v* and *w*-displacements. Therefore, in order to capture local variations in structural response, full-field displacement maps must be available. In fact, strains are more or less complicated combinations of displacement gradients. Furthermore, stress values are accurate only if the constitutive model is reliable. In view of the preceding discussion, a procedure directly based on displacements seems to be the most straightforward and robust approach to the identification of a whatever complex material behaviour.

Full-field displacement maps can be obtained with a great deal of accuracy by utilizing non-contact optical methods (NCOM) such as moiré, speckle and holography (Cloud, 1998; Sciammarella, 2003). For this reason, displacements are measured in this research with moiré techniques and then compared with numerical predictions provided by finite element models in order to identify constitutive behaviour of hyper-elastic membranes. The reverse engineering problem is formulated in fashion of an optimization problem where the unknown material properties are included as design variables. The cost function to be minimized is the error functional Ω built by summing over the differences between displacements measured experimentally and those predicted numerically. The material characterization process is hence a hybrid technique since it entails experimental measurements, finite element analysis and numerical optimization. The use of hybrid experimental–numerical techniques in identification problems is well documented in literature by several studies carried out on isotropic, composite and rubber materials under static and dynamic conditions (Sol et al., 1997; Cunha et al., 1999; Hwang and Chang, 2000; Rikards et al., 2001; Kang et al., 2004; Genovese et al., 2005, 2006; Martins et al., 2006; Pagnotta, 2006; Cugnoni et al., 2007).

Because of the continuous improvements in computing hardware, gradient based optimization utilizing local approximations has progressively been replaced by wide-range approximations utilizing response surfaces and by global optimization techniques such as simulated annealing – SA – (Kirkpatrick et al., 1983; Van Laarhoven and Aarts, 1987; Rao, 1996) and genetic algorithms – GA – (Goldberg, 1989; Rao, 1996), which perturb randomly the design variables. SA and GA certainly are the two most popular global optimization techniques because of their robustness and efficiency. Their use in material identification processes is justified by the high degree of non-linearity usually entailed by these problems which may make it impossible to build accurate approximations. Simulated annealing mimics the cooling process of melted materials while genetic algorithms mimic the process of natural selection. The random generation of trial points allows larger fractions of design space to be explored than in gradient-based optimization where sensitivity analysis and search of candidate designs are performed only in the neighbourhood of the design point about which the problem is approximated. Although GA seem superior over SA in view of the fact that operate on a population of designs while SA is a point-based algorithm which identifies only one design in each optimization iteration and than develops it, the "hill-climbing" capability which allows local minima to be by-passed is possessed only by simulated annealing.

Genovese et al. (2005, 2006) successfully utilized SA for characterizing composite laminates and latex membranes. However, their optimization routine defined only one candidate design in each iteration. Multi-point SA algorithms generating instead a population of candidate designs in each new iteration were developed more recently for structural optimization (Lamberti and Pappalettere, 2007; Lamberti, 2008) in order to speed up the optimization process and expand the search space. The above-mentioned multi-level and multi-point schemes have been modified in this study in order to reduce the number of structural analyses. In particular, the population size has been increased and the optimization algorithm now keeps memory of the best records determined in the previous annealing cycles. This is done because the computational cost of the optimization part of the mechanical characterization process may become too high especially in anisotropic hyper-elasticity identification problems where there are many unknown material parameters.

There is a basic issue that must be addressed when mechanical characterization of materials is attempted by using hybrid techniques. How many experimental data should be collected in order to ensure the uniqueness of the solution of the identification problem? This question becomes more and more important as the constitutive model deviates from linear elasticity and isotropy. Avril and Pierron (2007) pointed out that although it is possible to match experimental and numerical data over a limited set of control points, accuracy and robustness of the identification process increase with the number of data compared in the Ω functional. In general, processing only one displacement component or a limited amount of information rather than all of the 3D displacement maps will work well if there are few unknown material parameters but could lead to erroneous results when there are many material parameters such as it occurs in the case of anisotropic hyper-elasticity.

In view of the preceding discussion, in this research, each displacement component is measured independently and then compared with the corresponding values predicted by finite element analyses. For that purpose, an innovative experimental moiré setup is introduced. The new setup allows the 3D displacement information to be recovered with one single camera. Since moiré fringes result from the modulation of a grating attached to the specimen surface or projected onto it (Sciammarella, 1972, 2003; Patorski, 1993; Cloud, 1998), in this work, besides a square-dot grid printed on the specimen surface, another grating is simultaneously projected onto the specimen itself. As the specimen deforms under the applied loads, the two grids are independently modulated and the moiré setup becomes sensitive to all displacement components.

By processing the different clusters of harmonics contained in the frequency spectrum of the interferograms recorded by the camera, it is possible to recover the full-field map of each displacement component.

The simultaneous measurement of all 3D displacement components by means of the new moiré setup introduced in this research is an important generalization with respect to other hybrid procedures for mechanical characterization of materials, where the optical setups could measure only the target displacement component specifically considered in the identification problem. For example, Genovese et al. (2005, 2006) measured the in-plane displacement u for a composite specimen under three-point-bending and the out-of-plane displacement w for an inflated latex membrane. However, while the relative "simplicity" of those constitutive models (i.e., in-plane orthotropy and two-parameter Mooney–Rivlin hyper-elasticity) could justify the use of only one displacement component as target quantity, the anisotropic hyper-elastic constitutive models usually hypothesized for biological tissues will certainly require a much larger quantity of information to be processed in the optimization. The larger amount of information provided by the new moiré setup, together with a more efficient SA-based optimization routine, may allow the identification process to be completed successfully and with less computational effort.

The new framework described in this paper including 3D moiré measurements and improved fast multi-point simulated annealing is first calibrated for the "simple" case of isotropic hyper-elasticity and then tested in the much more complicated case of anisotropic hyper-elasticity. Two membranes are considered: respectively, a natural rubber specimen and a glutaraldehyde treated bovine pericardium patch (GTBP). The isotropic constitutive law hypothesized for the natural rubber is the two-parameter Mooney–Rivlin model (Mooney, 1940; Rivlin, 1948a,b). The GTBP specimen is instead modelled as a transversely isotropic material since micro-structural studies demonstrated that collagen fibres are normally distributed about a mean preferred fibre direction (Sacks and Chuong, 1998; Hiester and Sacks, 1998). Since structural uniformity is a fundamental requisite in bioengineering applications, the present assumption of transversely isotropic hyper-elasticity made for the GTBP patch sounds logical (see also the discussion on the relationship between fibre-splay and degree of anisotropy made in Freed et al. (2005)). The optimization is hence carried out with 17 variables: 16 unknown material constants and the orientation of collagen fibres.

The membranes are inflated by air at increasing pressure. Since displacement information encoded in moiré patterns are referred to the deformed configuration (Sciammarella, 1972, 2003) while the results of non-linear finite element analysis are referred to the global reference system, it is important to transform experimental data into their corresponding "global" quantities. Finally, the unknown material properties are determined by solving the reverse engineering optimization problem with improved fast multi-point simulated annealing.

Results of the characterization process demonstrate the very good efficiency of the proposed framework. For the isotropic rubber specimen, the values of MR constants are in very good agreement (less than 1% difference) with target values; furthermore, the residual percent error on target displacements is less than 3.5%. For the anisotropic specimen, the maximum error on hyper-elastic constants is about 3.5% and the residual error on displacements is less than 3.1%. As expected, the identification process is insensitive to the initial guess on material parameters. Conversely, the characterization process fails or becomes less accurate if target displacement values are referred to the deformed configuration.

2. Description of the identification procedure

The main steps of the hybrid characterization procedure described in this paper are summarized by the flow-chart in Fig. 1. A detailed description of each step is given in the following sections.

2.1. Principles of moiré techniques

Moiré techniques measure displacements by locating the interference fringes produced by two gratings: one on the specimen and one used as a reference (Cloud, 1998; Sciammarella, 2003). The grating can be directly applied to the specimen surface (Intrinsic Moiré, IM) or projected onto it (Projection Moiré, PM). While the reference grating remains unloaded and therefore keeps its original dimensions, the specimen grating deforms as the specimen is loaded. The resulting interference pattern is comprised of alternating bands, called moiré fringes. Interference fringes can be produced virtually by subtracting the two images recorded for the unloaded and loaded configurations. Fringes are iso-displacement *loci*. The sensitivity of a moiré setup represents the relative displacement between points lying on two adjacent fringes. Sharp changes in fringe topology or pattern frequency provide information on field in-homogeneities.

However, two facts must be carefully considered when moiré techniques are utilized (Sciammarella, 1972, 2003). In the first place, moiré fringes provide displacement values with respect to the deformed configuration (i.e., in the Eulerian reference system). Second, fringe patterns recorded by the camera are actually the projections of the moiré pattern in the image plane of the recording device. This statement can be easily understood if one considers that the specimen grating deforms because it is attached to the specimen surface. Therefore, transformations of coordinates must be performed in order to recover correctly displacement information.

The simple schematic of Fig. 2 explains why it is necessary to account for the difference between the "local" reference system relative to the deformed configuration and the "global" reference system relative to the unloaded configuration. For the sake of simplicity, the diametrical section of an inflated circular membrane clamped at its edges is taken into consideration since it reproduces the experimental test cases reported later in this paper. For instance, if the membrane
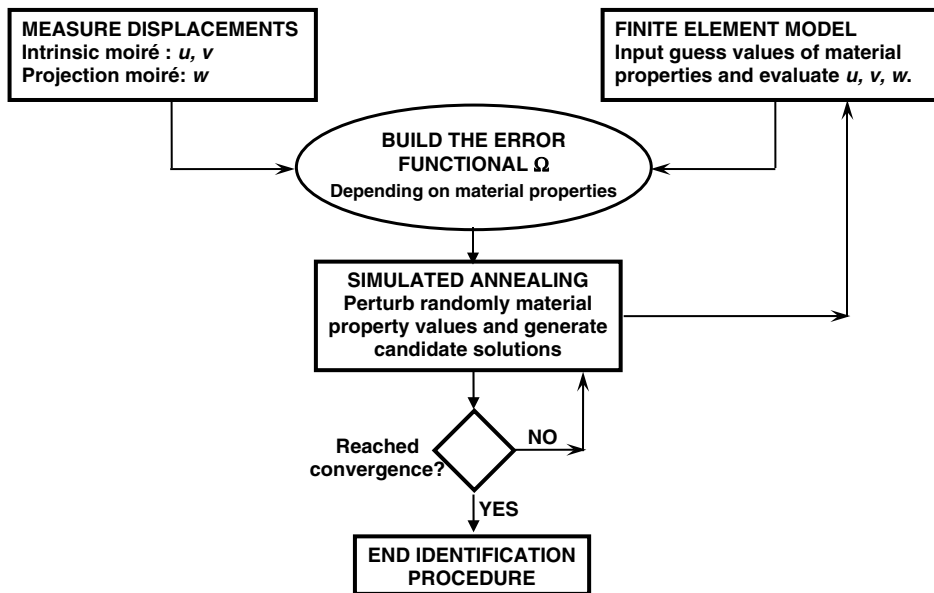
Fig. 1. Flow-chart of the hybrid characterization procedure used for hyper-elastic membranes.
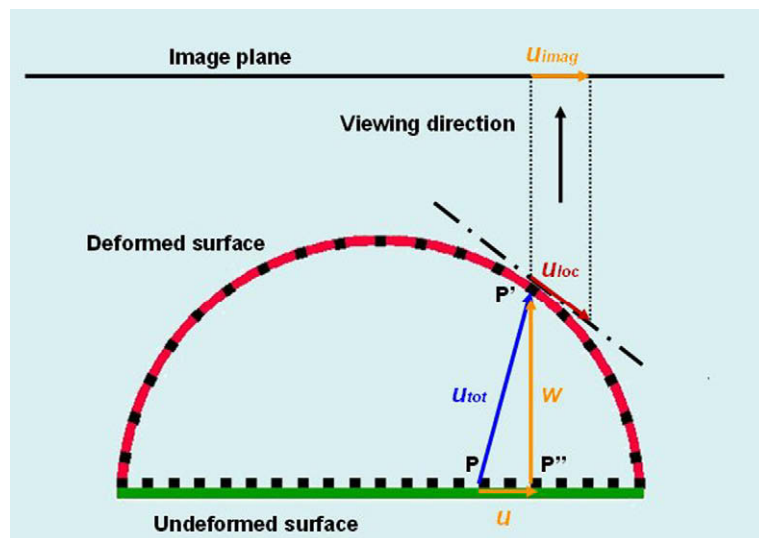

Fig. 2. Interpretation of displacement information encoded in moiré fringes.

is isotropic, because of the symmetry in loading and boundary conditions, specimen points lying on the diametrical plane of the membrane before deformation will remain on the same plane also during inflation. Therefore, only two displacement components (u and w) can be considered for the analysis. The generalization to the 3D case of anisotropic hyper-elasticity is indeed straightforward as all of the displacement components u, v and w will have to be considered.

The applied loads cause the point P to displace into the deformed position P'. Let us assume that a moiré fringe passes right through P'. Fringe order will be counted with respect to such deformed configuration. In the neighborhood of P' we can approximate the deformed surface to its tangent plane Π. This operation allows us to express, with respect to Π, the in-plane displacements measured by the modulated grating attached to the specimen surface. Let u_{loc} be the displacement component encoded by moiré fringes. As is clear, the difference between the "moiré" displacement u_{loc} and the real displacement u will become more significant as the deformation increases.

A similar argument can be made for the out-of-plane displacement values provided by the projection moiré fringe pattern. Each contour fringe represents a region of the specimen surface at a given distance from the reference plane corresponding to the undeformed configuration. The Lagrangian notation would hence imply that w is the out-of-plane
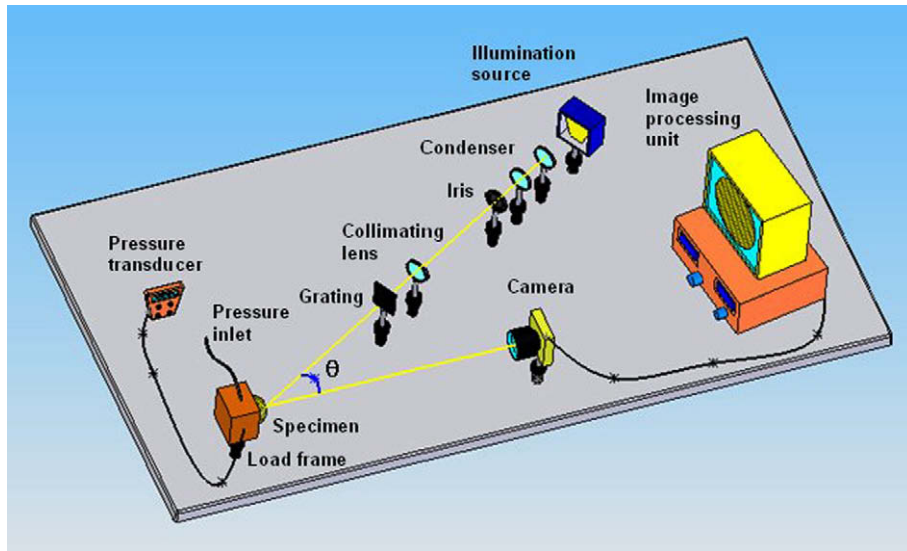
Fig. 3. Moiré setup used in the characterization process for measuring experimentally the whole 3D displacement field of the inflated membranes.

displacement of point P'' of the undeformed specimen. However, this is not true because the distance w between P' and the reference plane actually is the out-of-plane displacement of point P, not of P''. Therefore, the w-quantity evaluated at P' must be combined with the u-displacement experienced by P in order to determine correctly the total displacement u_{tot} of point P.

Another aspect to be considered is that moiré patterns are imaged in the image plane of the camera sensor. Each point of the image plane will hence correspond to a point of the object surface that has experienced some displacement. Generally speaking, each displacement component can be considered as a 3D surface depending from the spatial coordinates x, y and z. Let $u(x,y,z)$, $v(x,y,z)$ and $w(x,y,z)$ be the displacement functions. Fringe patterns imaged by the sensor represent the projections of the spatial functions u, v and w onto the image plane (see, for instance, the segment u_{imag} represented in Fig. 2). Therefore, 2D fringe patterns must be transformed into spatial distributions by using the 3D shape information of the deformed object.

2.2. Experimental measurements of 3D displacement field

The IMPM (intrinsic moiré & projection moiré) experimental setup used for measuring simultaneously all 3D displacement components is shown in Fig. 3. Since moiré techniques do not pose any limitation on the magnitude of displacements to be measured, they fit very well in the characterization procedure of hyper-elastic materials. In the case of isotropic hyperelasticity, the specimen is a natural rubber circular membrane (diameter = 40 mm, thickness = 1 mm), clamped by an O-ring seal attached to a pressurizing system nozzle, and progressively inflated. A controlled air pressure system provides 12 different load levels progressively increasing from 1.03 to 15.25 kPa. The anisotropic specimen is a circular patch of GTBP (diameter = 40 mm, thickness = 0.5 mm). The above mentioned loading conditions are slightly modified: the GTBP patch is submitted to 11 different load levels progressively increasing from 0.74 to 12.22 kPa.

A square-dot grating (pitch p_{IM} = 1 mm) has been printed by serigraphy on the surface of the rubber membrane in order to measure the in-plane displacements u and v with IM. At the same time, another grating (pitch p_{PM} = 2 mm) is projected onto the membrane in order to measure the out-of-plane displacement w with PM. The illuminating (white light) wave-front arrives collimated to the specimen surface since the exit pupil of the condenser lens system of the projector is located exactly in the focal plane of the collimating lens. The illumination angle θ_o (42.96°) can be measured by comparing the pitch $p_{PM,j}$ of

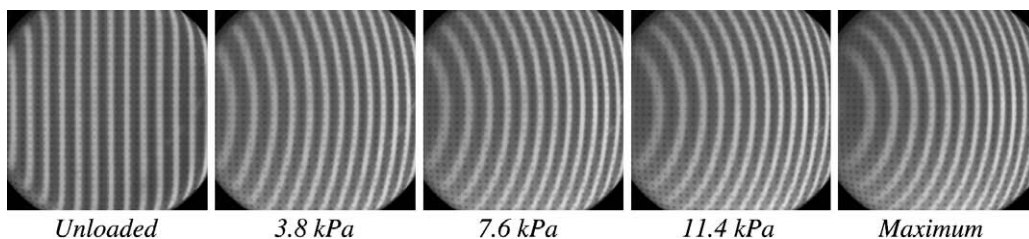*Unloaded* *3.8 kPa* *7.6 kPa* *11.4 kPa* *Maximum*

Fig. 4. Undeformed configuration and deformed configurations recorded for increasing pressures acting on the natural rubber membrane.

the grating projected onto the reference plane (i.e., the plane of the membrane in the unloaded state) with the nominal pitch of the grating p_{PM}. The value of the illumination angle is determined from the relationship $p_{PM,j} = p_{PM}/\cos\theta_o$.

In the case of the pericardium patch, another square-dot grating of pitch $p_{IM} = 1$ mm (i.e., the same grating used for the rubber membrane) has been applied to the membrane by simply laying down onto the sample surface an ink-jet printed sheet. The sticking surface of the wet membrane, in fact, rapidly absorbed the ink thus allowing a well defined dot pattern to be transferred from the paper to the sample. The illumination angle θ_o utilized in this experiment has been increased to 57.76° in order to obtain the best quality of fringes. Because of the large deflections experienced by the two membranes, a coarse grating could sample w-displacement values.

The two grids printed or projected onto the membrane are independently modulated as the specimen deforms under the action of the applied pressure. A 1280×1024 B/W CMOS camera recorded the images of the modulated gratings for each pressure level. Reference images of the unloaded specimens are also recorded by the camera. Fig. 4 shows the grating modulations observed for a set of different pressure levels acting on the rubber membrane (respectively, 0 – corresponding to the undeformed configuration; 3.8, 7.6, 11.4 and 15.25 kPa – the maximum pressure). For increasing pressures, the spatial frequency of the printed dots becomes larger while the lines projected onto the surface become more curved. The same behaviour has obviously been observed for the pericardium patch (see Fig. 5, showing the patterns for the unloaded membrane and the maximum pressure of 12.22 kPa).

The values of in-plane displacements can be determined from the classical IM equation

$$u, v = n_{u,v} \cdot p_{IM}, \tag{1}$$

where n_u and n_v are, respectively, the fringe orders of moiré patterns relative to X or Y-directions. From Eq. (1), it appears that the sensitivity value for the IM setup is equal to the pitch of the dot-grating printed onto the membrane.

The PM optical system is designed in such a way that projection (collimated light) and viewing are from infinity (telecentric lens system). This simplifies the mathematical model from which the out-of-plane displacements and hence the curvature of the inflated surface are computed. The height h of the surface with respect to the reference plane can be expressed as

$$h = n_w \cdot p_{PM} / \sin\theta_o, \tag{2}$$

where n_w is the fringe order of the projection moiré pattern. The sensitivity of the PM setup hence is $p/\sin\theta_o$: that is, 2.935 and 2.365 mm, respectively, for the rubber membrane and the bovine pericardium patch.

Eqs. (1) and (2) are the basic relationships used in moiré analysis. In order to transform fringe patterns into full-field continuous displacement maps, hence computing more precisely the global displacement map, the phase difference $\Delta\phi$ between the unloaded configuration and the modulated grating (Sciammarella, 2003) must be evaluated. It can be written as

$$\begin{aligned} u, v &= (\Delta\phi_{u,v}/2\pi) \cdot p_{IM} \\ h &= (\Delta\phi_h/2\pi) \cdot (p_{PM}/\sin\theta_o), \end{aligned} \tag{3}$$

where the subscripts u, v and h are relative to the different displacement components. As previously remarked, all displacement components must be finally expressed in the global reference system.

All moiré patterns recorded in this study have been processed with the Holo Moiré Strain Analyzer™ (HMSA) Version 2.0 fringe analysis software package developed by Sciammarella and his collaborators and supplied by General Stress Optics Inc., Chicago (IL), USA. The HMSA package includes a very detailed library of state-of-the-art fringe processing tools based on Fourier analysis (fast Fourier transform, filtering, carrier modulation, fringe extension, edge detection and masking operations, removal of discontinuities, etc.). The software has been continuously developed over the years and can deal practically with any kind of interferometric patterns. The reader can refer to the classical paper by Sciammarella (2003) and to the GSO company website (General Stress Optics, 2008) for an overview of the many successful applications of the HMSA software in the fields of experimental solid-mechanics, measurement science and technology: large-scale components (displacement measurements, shape contouring, determination of buckling loads of aircraft panels, etc.), damage detection and monitoring of natural frequencies (fracture of turbine blades for jet engines, auxiliary power generators of space vehicles, particle-reinforced composites, etc.), micro-components (electronic chips, solid propellant particles, etc.), nano-scale measurements (optical super-resolution problems, detection of nano-crystals, etc.), high precision contouring, etc.
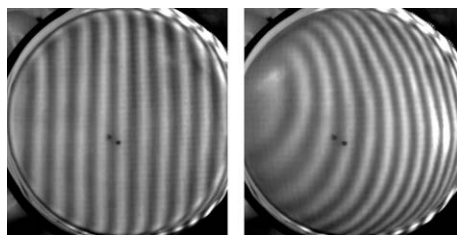

Fig. 5. Undeformed configuration and deformed configuration recorded for the maximum pressure (12.22 kPa) acting on the bovine pericardium patch.
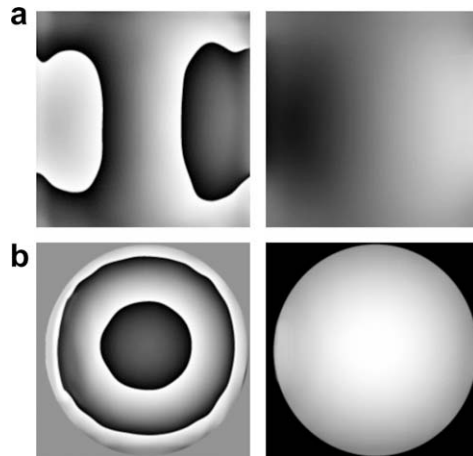
Fig. 6. Wrapped phase map and displacement field of the inflated natural rubber membrane: (a) in-plane and (b) out-of-plane.

The different steps required for processing moiré patterns with HMSA now are briefly summarized. The images of the reference and modulated gratings recorded by the camera are transformed into 1024×1024 square images. Then, each fringe pattern is filtered in the frequency space. Harmonics corresponding to each displacement component can be easily separated because of the large difference in frequency between the IM and PM gratings selected for the present experiments. Phase distributions of the reference grating and of the modulated grating are obtained using the in-quadrature filter. Then, phases are subtracted each other in order to obtain the phase $\Delta\phi$ of the equivalent moiré fringes. The resultant phase distribution is modulated by a 128 frequency carrier and filtered again. Finally, full-field displacement maps are obtained through unwrapping. More details on the fringe processing operations can be found in the classical paper published by Sciammarella (2003).

Fig. 6 shows the phase distribution and the corresponding displacement field obtained for the maximum pressure (15.25 kPa) applied to the natural rubber membrane. The in-plane displacement field (Fig. 6a) has been obtained by processing the harmonics corresponding to the square-dot grid pattern while the out-of-plane displacement field (Fig. 6b) has been obtained by processing the projected fringe pattern. Because of load symmetry, distributions of u and v displacements obviously coincided in shape. The largest in-plane displacement was 1.1 mm while the largest out-of-plane displacement was 8.85 mm.

Fig. 7 summarizes the results obtained for the maximum pressure load applied to the pericardium patch. The FT pattern shown in Fig. 7a again reveals the presence of three well distinct families of fringes. The first family – the one of highest intensity overall – portrays the modulation of the projected grating (i.e., the large circles centred on the horizontal axis of the frequency space). The other two families describe the modulation of the square-dot grating printed on the specimen surface (i.e., the small circles displaced with respect to the FT coordinate axes). Since these fringes are inclined with respect to both horizontal and vertical directions (see Fig. 7b), the GTBP patch is not isotropic. Conversely, the in-plane displacement phase patterns obtained for the natural rubber membrane are perfectly symmetric about coordinate axes X and Y (see Fig. 6) because they derive from two families of horizontal and vertical fringes. By composing the two families of oblique fringes in Fig. 7b, one can obtain a family of ellipses whose major axis is inclined by the angle θ_f corresponding to the direction of collagen fibres (see Fig. 7b). Further evidence of this can be gathered from the phase pattern reconstructed by extracting the harmonics corresponding to the modulation of the projected grating (see Fig. 7c). There is a clear difference between this w-displacement phase map and its counterpart obtained for the natural rubber membrane (see Fig. 6b). In the GTBP case, phase contour lines are again ellipses with the same orientation shown by total in-plane displacement contour lines. Conversely, the w-displacement phase map obtained for the natural rubber specimen is circularly shaped as it was expected for an inflated isotropic membrane. The largest in-plane displacement measured for the GTBP patch was about 0.5 mm while the largest out-of-plane displacement was about 5.3 mm.

Experimental data have finally been expressed in the global reference system by following the principles illustrated in Fig. 2 and outlined in the preceding section. This operation is required in order to correctly compare the experimental results with numerical predictions within the hybrid characterization process described in this paper.

2.3. Finite element modelling and analysis of the inflated membranes

Finite element modelling and analysis of the hyper-elastic membranes have been carried out with the ANSYS® Version 10.0 general purpose FEM software developed by ANSYS Inc., Canonsburg, PA, USA. The FE model of the rubber membrane is shown in Fig. 8: the mesh is comprised of 1200 SHELL181 hyper-elastic elements and includes 1241 nodes. The FE model of the pericardium patch is instead comprised of 1200 quadratic SOLID186 hyper-elastic elements and includes 8603 nodes. Quadratic solid elements allowed the transverse stiffness of the membrane to be increased thus avoiding numerical
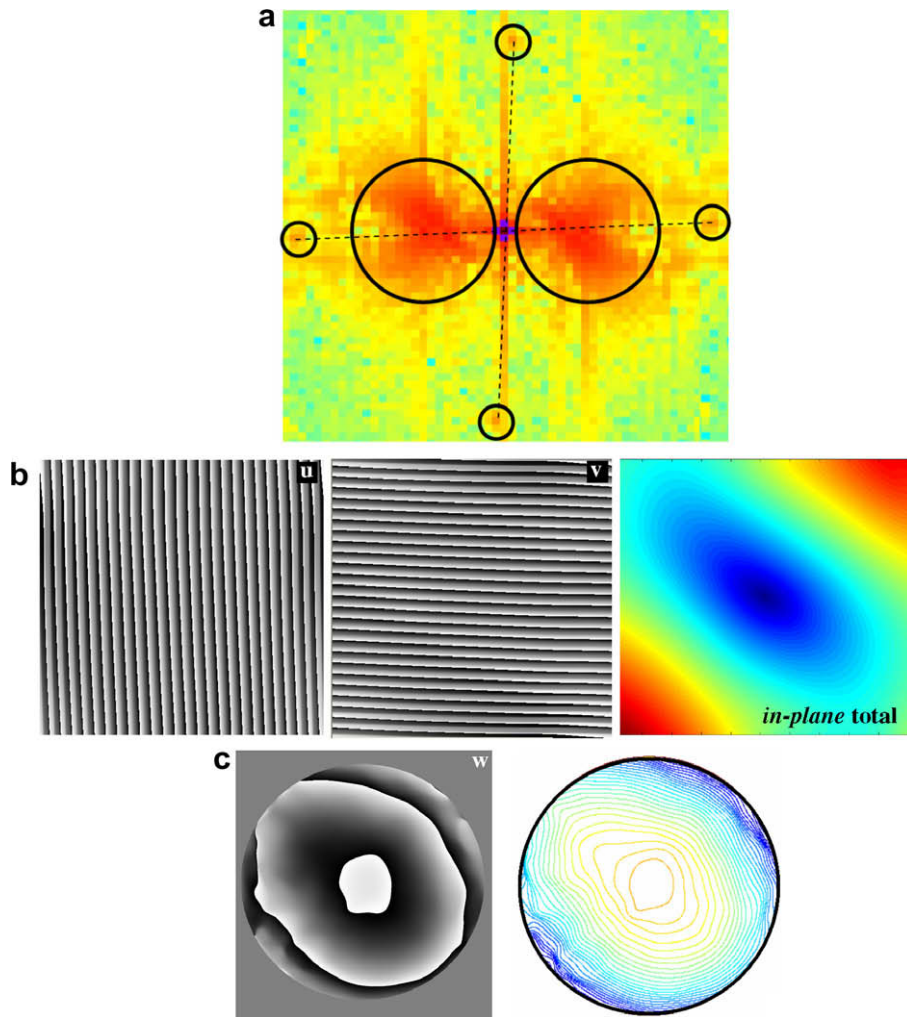
Fig. 7. Bovine pericardium patch: (a) FT of fringe pattern; (b) phase map of in-plane displacements and corresponding color map of the resultant in-plane displacement; and (c) unfiltered phase map of out-of-plane displacements and corresponding contour lines.

instability problems in the execution of finite element analyses. This modelling choice is justified by the fact that the thickness of the pericardium patch is half of the thickness of the natural rubber specimen (i.e., 0.5 vs. 1 mm). Since both specimens have the same radius (i.e., 20 mm) and the same grating was printed onto them, the corresponding FE models have the same element size in the plane of the membrane.

The natural rubber membrane has been modelled as an isotropic-incompressible hyperelastic material following the two-parameter Mooney–Rivlin (MR) constitutive equation. The corresponding strain energy density function is

$$W = a_{10}(\bar{I}_1 - 3) + a_{01}(\bar{I}_2 - 3), \tag{4}$$

where a_{10} and a_{01} are the Mooney–Rivlin constants given in input to ANSYS as material properties. Strain invariants are defined, respectively, as $\bar{I}_1 = \text{tr}[C]$ and $\bar{I}_2 = \{\text{tr}^2[C] - \text{tr}^2[C]^2\}$, where $[C]$ is the Cauchy–Green strain tensor.

The anisotropic GTBP membrane has been modelled as a transversely isotropic hyper-elastic material. The strain energy density function W depends on nine strain invariants, $\bar{I}_i$ $(i = 1, \ldots, 9)$. The first three invariants defined, respectively, as $\bar{I}_1 = \text{tr}[C]$, $\bar{I}_2 = \{\text{tr}^2[C] - \text{tr}^2[C]^2\}$ and $\bar{I}_3 = \det[C]$, correspond to isotropic hyper-elasticity (i.e., Mooney–Rivlin, Yeoh, Arruda-Boyce, Gent, Blatz-Ko, Ogden Potential models, etc.). The other six strain invariants, defined, respectively, as $\bar{I}_4 = \mathbf{A} \cdot [C]\mathbf{A}$, $\bar{I}_5 = \mathbf{A} \cdot [C]^2\mathbf{A}$, $\bar{I}_6 = \mathbf{B} \cdot [C]\mathbf{B}$, $\bar{I}_7 = \mathbf{B} \cdot [C]^2\mathbf{B}$, $\bar{I}_8 = (\mathbf{A} \cdot \mathbf{B})\mathbf{A} \cdot [C]\mathbf{B}$ and $\bar{I}_9 = (\mathbf{A} \cdot \mathbf{B})^2$, account for material anisotropy. For fibrous hyper-elastic materials like GTBP, "isotropic" behaviour is associated with matrix properties while "anisotropic" behaviour is associated with fibre properties and fibre/matrix interactions. In order to account for these effects, material microstructure is defined in ANSYS 10.0 by assigning two directions **A** and **B** whose orientations are specified with respect to the undeformed configuration.
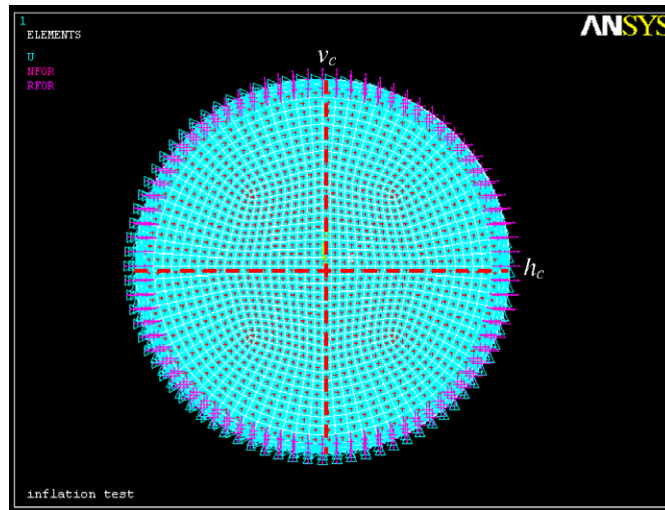
Fig. 8. Finite element model of the inflated membranes. Natural rubber and GTBP specimens have the same radius but different thickness. Control paths h_c and v_c also are sketched.

The strain energy density function W can be decomposed in two parts: the volumetric term W_v and the deviatoric term W_d. The deviatoric term can be further decomposed in a term $W_{d,iso}$ related to isotropic behaviour and in another term $W_{d,aniso}$ related to anisotropic behaviour. It follows:

$$W = W_v + W_{d,iso} + W_{d,aniso}. \tag{5}$$

The volumetric term W_v is directly dependent on the third strain invariant $\bar{I}_3$ in fashion of $W_v = (\bar{I}_3 - 1)^2/d$ where the d parameter is equal to 0 for fully incompressible behaviour.

The "isotropic" deviatoric term $W_{d,iso}$ depends on the first two strain invariants $\bar{I}_1$ and $\bar{I}_2$: it is hence similar to the general polynomial form used in isotropic hyper-elasticity:

$$W_{d,iso} = \sum_{i=1}^{3} a_i(\bar{I}_1 - 3)^i + \sum_{j=1}^{3} b_j(\bar{I}_2 - 3)^j, \tag{6}$$

where the six constants a_i and b_j are specified in input to ANSYS as material properties.

The "anisotropic" deviatoric term $W_{d,iso}$ is again similar to the general polynomial form used in isotropic hyper-elasticity, but depends on strain invariants $\bar{I}_4$, $\bar{I}_5$, $\bar{I}_6$, $\bar{I}_7$, $\bar{I}_8$ and $\bar{I}_9$, which are function of the microstructure property vector **A**. That is

$$W_{d,aniso} = \sum_{k=2}^{6} c_k(\bar{I}_4 - 3)^k + \sum_{l=2}^{6} d_l(\bar{I}_5 - 3)^l + \sum_{m=2}^{6} e_m(\bar{I}_6 - 3)^m + \sum_{n=2}^{6} f_n(\bar{I}_7 - 3)^n + \sum_{o=2}^{6} g_o(\bar{I}_8 - \bar{I}_9)^o, \tag{7}$$

where the 25 constants c_k, d_l, e_m, f_n and g_o also are given in input as material properties.

Eq. (7) becomes simpler for a transversely isotropic material because $\bar{I}_6, \bar{I}_7, \bar{I}_8, \bar{I}_9 = 0$ as the microstructure direction **B** is null. Therefore, constants e_m, f_n and g_o are no longer required in structural analysis. In summary, 16 hyper-elastic constants as well as the orientation of the reinforcing fibres must be determined in the identification process of the pericardium patch.

Convergence analysis has been carried out in order to have mesh independent solutions. Element distribution is such to keep the correspondence between nodes of the FE model and the grating-dots printed on the inflated membrane. Fig. 8 shows also the pressure load acting on the two membranes and the zero-displacement constraints applied along the circular edge.

Finite element analyses obviously accounted for the large deformations experienced by the hyper-elastic membranes. The geometric non-linearity option is activated by switching on the NLGEOM command. Non-linear analysis has been divided in 12 load steps for the isotropic specimen and in 11 load steps for the anisotropic membrane. Each load step solved in ANSYS corresponds to a different pressure level applied to the membrane. Comparisons between displacement maps shown, respectively, in Figs. 6 and 9 (rubber specimen) and in Figs. 7 and 10 (pericardium patch) prove the good agreement between experimental measurements and FE predictions for both the isotropic and anisotropic specimens considered in this study. The circular symmetry exhibited by the displacement maps obtained for the isotropic specimen does not exist any more for the anisotropic specimen which instead shows displacement maps shaped as ellipses inclined with respect to coordinate axes.

2.4. Formulation of the inverse problem: matching of moiré data and FEM predictions

The different displacement components measured with IM and PM have been matched to finite element predictions in order to determine material properties of the two hyper-elastic membranes. Displacement components have been summed
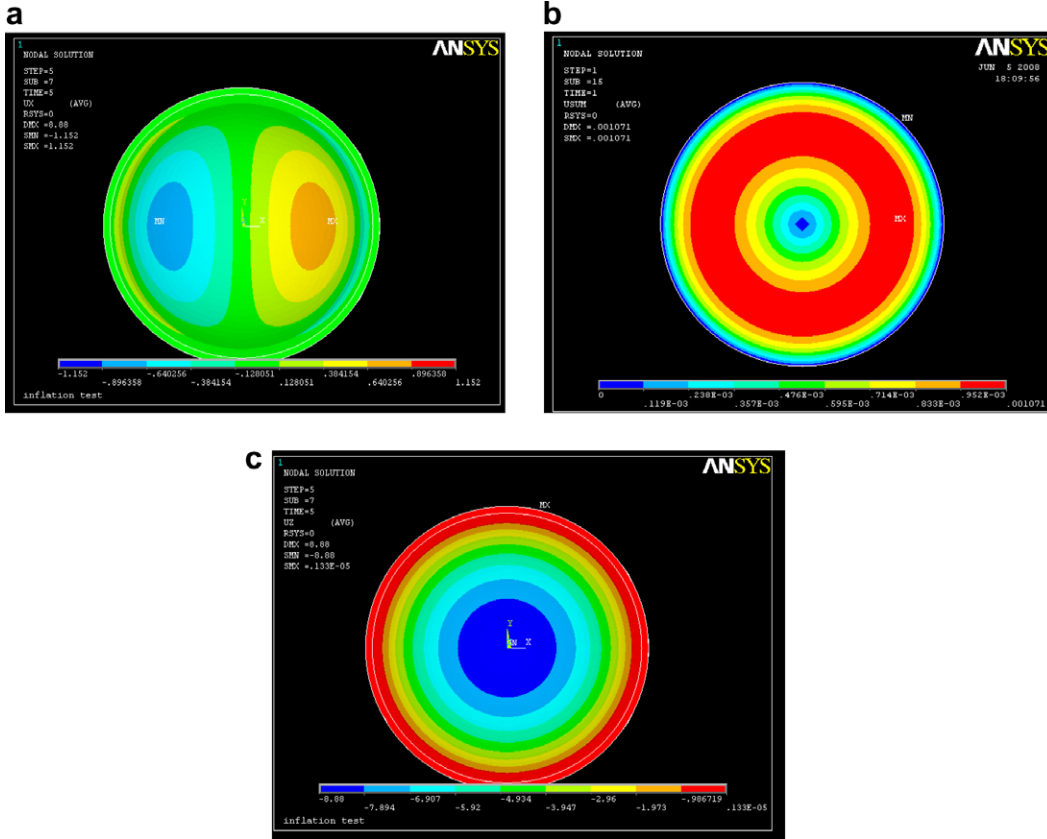
Fig. 9. Natural rubber membrane. Finite element predictions of displacement fields: (a) in-plane *u*; (b) total in-plane; and (c) out-of-plane *w*.

over into the total displacement $u_{\text{tot}} = \sqrt{u^2 + v^2 + w^2}$, expressed with respect to the origin of the global coordinate system. Let N_{CNT} be the number of control points at which experimental data and numerical predictions are compared. Also, let $\bar{u}^j_{\text{tot}}$ and u^j_{tot} be the total displacements evaluated in correspondence of the jth control point, respectively, for the experimental and numerical data.

The measured displacements $\bar{u}^j_{\text{tot}}$ are taken as target values since moiré experimental tests can be carried out without knowing material properties *a priori*. Conversely, hyper-elastic constants must be given in input to FE analysis in order to calculate displacements. As is clear, numerical predictions can match experimental results only if the right material property values are given in input to the FE model. For this reason, the mechanical characterization problem becomes a non-linear optimization problem, whose formulation changes if the hyper-elastic specimen to be characterized is isotropic or anisotropic. For the natural rubber membrane, it is

$$
\text{Min}\left[\Omega(a_{10}, a_{01}) = \sqrt{\frac{1}{N_{\text{CNT}}} \sum_{j=1}^{N_{\text{CNT}}} \left(\frac{u^j_{\text{tot}} - \bar{u}^j_{\text{tot}}}{\bar{u}^j_{\text{tot}}}\right)^2}\right],
$$
$$
a^l_{10} \leqslant a_{10} \leqslant a^u_{10},
$$
$$
a^l_{01} \leqslant a_{01} \leqslant a^u_{01},
$$
(8)

where the two unknown Mooney–Rivlin constants a_{10} and a_{01} are included as design variables. As is mentioned in Section 2.1, because of load symmetry and specimen isotropy, the total displacement u_{tot} reduces to $\sqrt{u^2 + w^2}$. Additional constraints, such as the positive definiteness of tangential material stiffness, ensure stability of the non-linear material. The lower bounds of hyper-elastic constants have been set as 80 kPa for a_{10} and 1 kPa for a_{01}; upper bounds have been set as 1 MPa for a_{10} and 200 kPa for a_{01}.

The control path chosen for matching experimental results and numerical predictions coincides with the horizontal diameter of the inflated membrane (i.e., the red etched line h_c in Fig. 8). As is said previously, nodes of FEM model correspond to the grating dots printed onto the membrane. Therefore, the Ω functional is built by summing over the errors on displacements evaluated at $N_{\text{CNT}} = 41$ control points. Should node spacing not coincide with the grating pitch, this would not be a major problem. In fact, moiré data are available in a continuous fashion from the unwrapping operation.
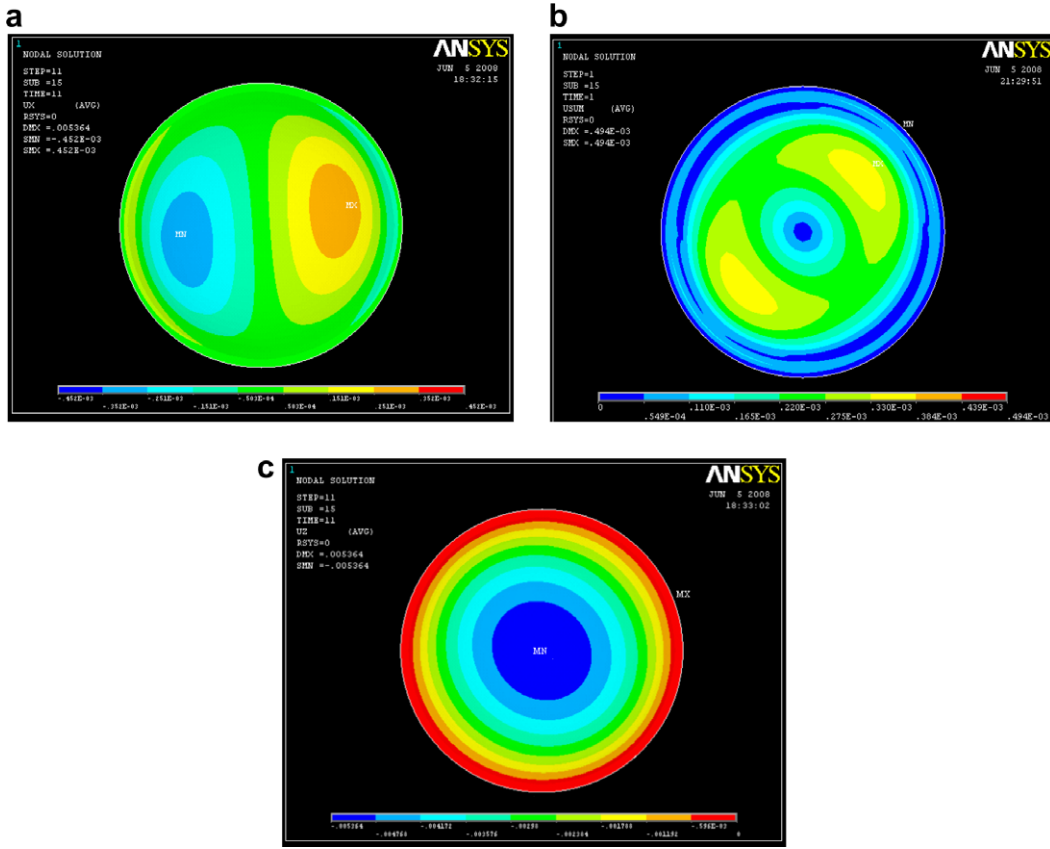
Fig. 10. Bovine pericardium patch. Finite element predictions of displacement field: (a) in-plane u; (b) total in-plane; and (c) out-of-plane w.

The error functional Ω has been minimized with the new fast multi-point simulated annealing algorithm presented in this paper. In order to check the robustness of the identification algorithm, six optimization runs have been conducted by matching different displacement components or/and starting from different initial values of the MR constants. As far as it concerns displacements, u and w displacements have been considered singularly as the target quantities or combined together into the global displacement u_{tot}; v displacements can be obviously neglected since the control path lies on the membrane diameter. Optimizations have been started from two different points: $a_{10} = 80$ kPa, $a_{01} = 1$ kPa (Run A) and $a_{10} = 1$ MPa, $a_{01} = 200$ kPa (Run B).

For the bovine pericardium patch, the identification problem, again solved with the new SA-based algorithm presented in this paper, can be instead formulated as follows:

$$
\text{Min}\left[\Omega(a_{1,2,3}; b_{1,2,3}; c_{2,3,4,5,6}; d_{2,3,4,5,6}; \cos\theta) = \sqrt{\frac{1}{N_{\text{CNT}}} \sum_{j=1}^{N_{\text{CNT}}} \left(\frac{u_{\text{tot}}^j - \overline{u}_{\text{tot}}^j}{\overline{u}_{\text{tot}}^j}\right)^2}\right],
$$

$$
a_{1,2,3}^l \leqslant a_{1,2,3} \leqslant a_{1,2,3}^u,
$$
$$
b_{1,2,3}^l \leqslant b_{1,2,3} \leqslant b_{1,2,3}^u,
$$
$$
c_{2,3,4,5,6}^l \leqslant c_{2,3,4,5,6} \leqslant c_{2,3,4,5,6}^u,
$$
$$
d_{2,3,4,5,6}^l \leqslant d_{2,3,4,5,6} \leqslant d_{2,3,4,5,6}^u,
$$
$$
\cos\theta^l \leqslant \cos\theta \leqslant \cos\theta^u,
$$

(9)

where the 16 hyper-elastic constants and fibre orientation direction cosine $\cos\theta$ are included as design variables: hence, there are 17 unknown material properties. The total displacement u_{tot} is computed as $\sqrt{u^2 + v^2 + w^2}$. Upper and lower bounds of hyper-elastic constants are set as 10 kPa and 1 MPa, respectively. The direction cosine $\cos\theta$ defining the orientation of the collagen fibres can range between 0.65 and 0.75. Two optimization runs have been carried out: Run A starting from the uniform design of 10 kPa (i.e., variable lower bound) and Run B starting from the uniform design of 1 MPa (i.e., variable upper bound); in both cases, $\cos\theta$ has been initially set equal to 0.7.

In order to account for the specimen anisotropy, experimental results and numerical predictions have been matched along both horizontal and vertical diameters of the GTBP patch (i.e., the etched red lines h_c and v_c in Fig. 8) because all displacement components are different from 0. Therefore, a total of 81 control points have been considered in the optimization process. Since directions of control paths do not coincide with material directions (in fact, displacement fringes are inclined with respect to coordinate axes), the identification process is absolutely general.

2.5. Determination of target values of hyper-elastic constants

Since this research aims to demonstrate that it is possible to characterize hyper-elastic membranes by matching 3D displacement components simultaneously measured by the IMPM system with numerical predictions, complementary experimental campaigns based on planar equi-biaxial testing (PEBT) have been conducted on the investigated specimens in order to determine independently their material properties. As is clear, these complementary campaigns could have been omitted if the hybrid identification procedure was tested on materials for which constitutive parameters are known *a priori*. However, carrying out independently two experimental campaigns certainly gives more generality and robustness to the hybrid identification procedure described in this paper.

The PEBT experimental apparatus shown in Fig. 11 is shaped as a frame onto which there are mounted 12 linear slide guides and 12 loose pulleys. At the extremities of the mobile parts of each linear slide there are two screwed holes of 2.6 mm diameter: one serves to fix the membrane while the other bears the flexible thread where calibrated weights are applied. Linear guides force the boundary of the membrane to expand in the radial direction thus generating the equi-biaxial state in the centre of the specimen. Seven different calibrated weights – from 50 to 500 g for the rubber membrane and from 50 to 600 g for the pericardium patch – have been applied to the specimens in order to cause the progressive deformation of the membrane.

Specimen deformations and displacements have been monitored with a very simple intrinsic moiré setup (Genovese et al., 2006; Cosola et al., 2008) where the camera is orthogonal to the plane where membranes deform. The dot-gratings have been applied onto specimens as is described in Section 2.2. All moiré patterns have been processed with the HMSA software. Because of loading and constraint conditions, no out-of-plane displacements could occur during the biaxial test. In
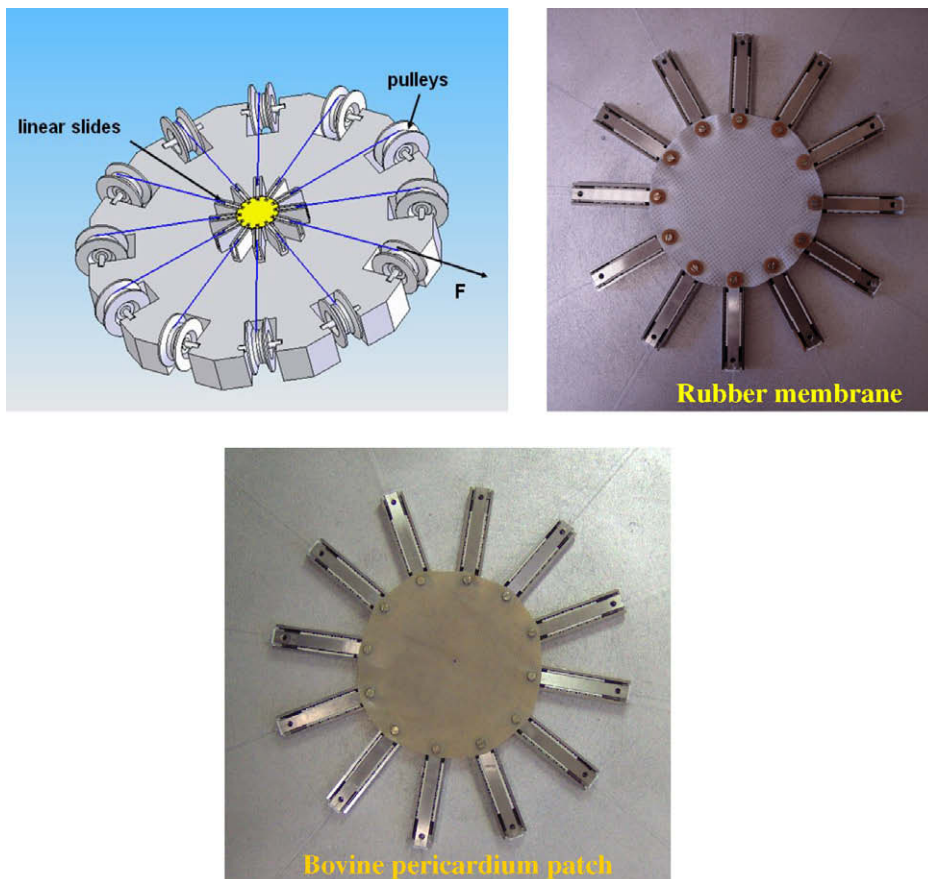

Fig. 11. Schematic and detailed view of the planar equi-biaxial testing apparatus for determining target values of material properties.

order to ensure load uniformity thus avoiding effects of apparent anisotropy, the 12 flexible threads have been blocked by a hard rubber ring pressed against the testing apparatus by a vertical force. The stiff ring is slightly removed after that all dead weights are applied to the membrane.

For the natural rubber specimen, the target values of Mooney–Rivlin constants have been computed by the ANSYS program through fitting of engineering stresses and strains. For each weight load, the corresponding engineering stress σ generated inside the region delimited by the inner diameter $D_i = 68$ mm can be determined as $\sigma = F/\pi D_i t$, where F is the radial force resultant and t is the specimen thickness. True strain values corresponding to the frequency of the IM fringe pattern have been converted into engineering strains. The target material properties resulting from the fitting process are: $a_{10} = 201.021$ kPa and $a_{01} = 13.201$ kPa.

However, this simple fitting procedure could not be utilized for the pericardium patch because of the anisotropy of the biological tissue. Therefore, the in-plane displacements u and v have been taken as target displacements and an optimization problem similar to that described by Eq. (9) has been formulated and solved. The total displacement u_{tot} has been obviously computed as $\sqrt{u^2 + v^2}$. The optimization process started from the uniform initial design of 0.1 MPa for all hyper-elastic constants and $\cos\theta = 0.7$ in order to ensure fast convergence of finite element analyses. The different steps of the calibration campaign are described with a great deal of detail in Cosola et al. (2008). The following material properties have been determined for the GTBP patch: $a_1 = 199.357$, $a_2 = 126.334$, $a_3 = 135.041$, $b_1 = 387.799$, $b_2 = 170.465$, $b_3 = 186.066$, $c_2 = 197.786$, $c_3 = 89.976$, $c_4 = 174.898$, $c_5 = 169.682$, $c_6 = 148.472$, $d_2 = 158.028$, $d_3 = 21.405$, $d_4 = 69.605$, $d_5 = 165.645$, $d_6 = 101.767$ kPa and $\cos\theta = 0.6833$ corresponding to $133.1°$ fibre inclination with respect to the X-axis. These values have then been given in input to a finite element model simulating the inflation test later executed. A good agreement between the displacement values measured with the projection moiré setup and those predicted by the numerical model has been observed. However, the verification process carried out in the calibration phase did not considered as target the total displacements expressed in the global reference system, but directly compared only the out-of-plane displacement component resulting from PM measurements.

2.6. Solution of the inverse problem: the optimization algorithm

The pseudo-code of the new SA-based optimizer used in this research is now provided. The optimization code implements a multi-level and multi-point architecture. In each iteration, a population of candidate designs is generated
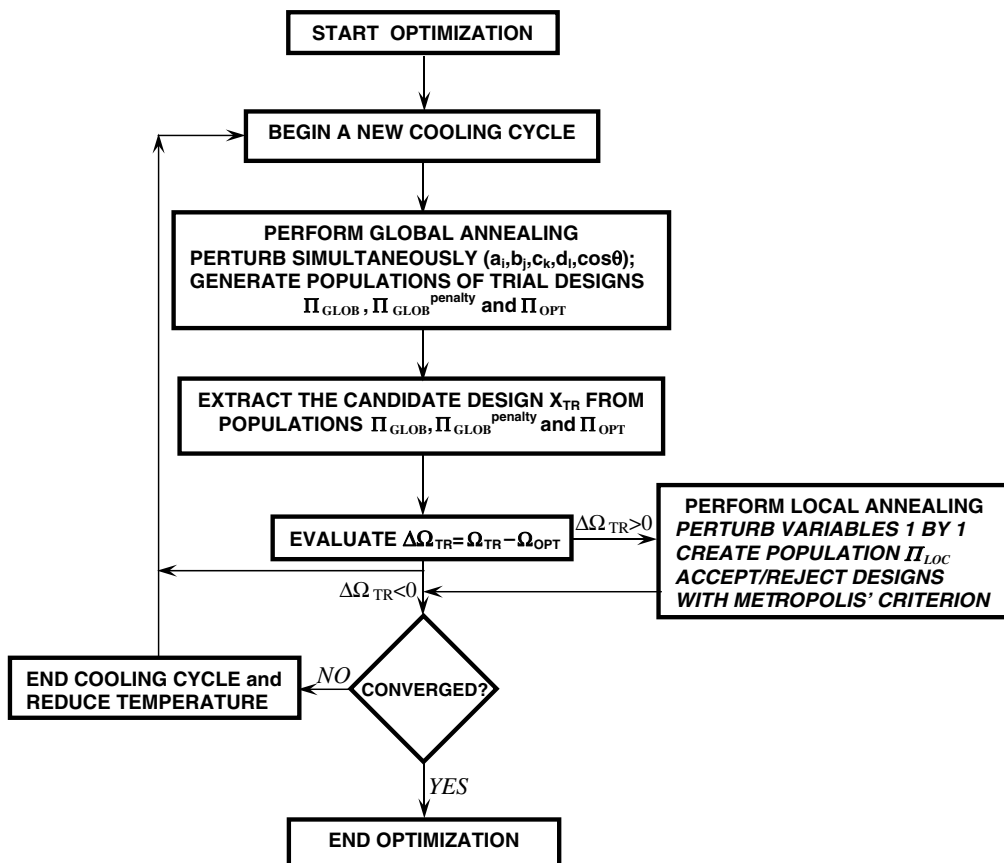

Fig. 12. Flow chart of the simulated annealing algorithm used in the characterization process.

by perturbing all optimization variables simultaneously or one at a time. More details on the theoretical foundation of the present optimization algorithm can be found in Genovese et al. (2005), Lamberti and Pappalettere (2007), and Lamberti (2008). Those original formulations have been modified in this paper and adapted to the mechanical characterization of hyper-elastic membranes in order to improve the convergence behaviour of the optimization search thus reducing the corresponding computational cost in the case of material anisotropy. The most significant improvement with respect to the previous SA formulations is that larger populations of candidate designs are now considered in each optimization cycle. Furthermore, the new algorithm now keeps memory of the evolution of the optimization process by storing each current best record in a database from which additional design variable values can be extracted. The flow-chart of the SA-based algorithm is shown in Fig. 12.

Step 1. Start the optimization process. Set initial values of algorithm parameters.

As is stated in Section 2.4, the number N of design variables is, respectively, equal to 2 or 17 for the rubber membrane and the pericardium patch. If the rubber membrane is to be characterized, store the Mooney–Rivlin constants in the design vector $\mathbf{X}(a_{10}, a_{01})$. In the case of pericardium patch, store material properties in the design vector $\mathbf{X}(a_1, a_2, a_3, b_1, b_2, b_3, c_2, c_3, c_4, c_5, c_6, d_2, d_3, d_4, d_5, d_6, \cos\theta)$. Choose the initial design and store it in the vector $\mathbf{X}_{\text{OPT}}$ corresponding to the point P_{OPT} of design space. Denote as Ω_{OPT} the corresponding value of the error functional. Set as $K = 1$ the counter of cooling cycles.

Set the initial temperature as $T_o = 1000$. This value is much larger than the expected value of Ω – which must be close to 0 – in order to ensure that the acceptance probability threshold may be large enough throughout the optimization process. This strategy allows in principle to limit the number of trial designs rejected in each cooling cycle.

Step 2. Global annealing search. Generate the population of candidate designs.

In the global annealing search, trial designs are generated by perturbing simultaneously all material parameters. Each design variable x_i ($i = 1, \ldots, N$) is randomly perturbed as follows:

$$\partial\Omega/\partial x_i > 0 \Rightarrow \Delta x_i = -(x_i^u - x_i^l)N_{\text{RND},i}\mu_i\Omega_{\text{OPT},l}/\Omega_{\text{OPT},l-1},$$
$$\partial\Omega/\partial x_i < 0 \Rightarrow \Delta x_i = (x_i^u - x_i^l)N_{\text{RND},i}\mu_i\Omega_{\text{OPT},l}/\Omega_{\text{OPT},l-1}, \tag{10}$$

For each variable, the random number $N_{\text{RND},i}$ is chosen in the interval $(0, 1)$. Each weighting coefficient μ_i is defined as $|\partial\Omega/\partial x_i|/\|\bar{\nabla}\Omega(\mathbf{X}_{\text{OPT}})\|$ and is obviously smaller than 1. The weighting coefficients provide information on the effect of each variable in the optimization process and are computed as

$$\sum_{j=1}^{N_{\text{CNT}}} \left(\frac{u_{\text{tot}}^j - \bar{u}_{\text{tot}}^j}{\bar{u}_{\text{tot}}^j}\right) \frac{\partial u_{\text{tot}}^j}{\partial x_i} \bigg/ \sqrt{N_{\text{CNT}} \cdot \Omega(x_{\text{OPT},1}, x_{\text{OPT},2}, \ldots, x_{\text{OPT},i}, \ldots, x_{\text{OPT},N})},$$

where $i = 1, 2$ for the rubber membrane, while $i = 1, \ldots, 17$ for the pericardium patch. The partial derivatives $\partial u_{\text{tot}}^j/\partial x_i$ are evaluated with centred finite differences ($\delta x_i = x_{\text{OPT},i}/10{,}000$).

The $\Omega_{\text{OPT},l}$ and $\Omega_{\text{OPT},l-1}$ terms are the last two current best record values taken by the cost function. If the cost function decreases in two successive iterations, the ratio $\Omega_{\text{OPT},l}/\Omega_{\text{OPT},l-1}$ is greater than 1. The $\Omega_{\text{OPT},l}/\Omega_{\text{OPT},l-1}$ ratio hence is a sort of adjustment parameter which forces the optimizer to take movements large enough to maintain at least the current rate of reduction in cost function. This strategy allows the number of optimization iterations to be reduced substantially with respect to other SA implementations (Lamberti, 2008).
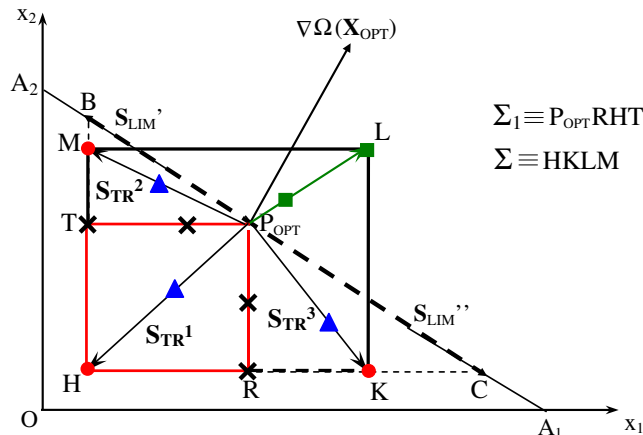

Fig. 13. Trial design generation in the SA-based optimization process.

The Δx_i movements set with Eq. (10) define the first descent direction $\mathbf{S}_{\mathrm{TR}}^1(\Delta x_1, \Delta x_2, \ldots, \Delta x_N)$, which is the diagonal of the Σ_1 domain (the P_{OPT} RHT rectangle in Fig. 13 for the simpler case of isotropic hyper-elasticity where there are two optimization variables). Other portions of design space must be added to Σ_1 in order to form a population of candidate designs for which there is some probability of reducing the error functional Ω. For this purpose, a set of descent directions is defined. Fig. 13, again for the simpler case of isotropic hyper-elasticity, shows that any descent direction has to lie below the segment $\overline{A_1 A_2}$, which is orthogonal to the gradient vector $\overline{\nabla}\Omega(\mathbf{X}_{\mathrm{OPT}})$. The unknown movements $\Delta x_1^{\lim}$ and $\Delta x_2^{\lim}$ that define, respectively, the two "limit directions" $\mathbf{S}_{\mathrm{LIM}}''$ and $\mathbf{S}_{\mathrm{LIM}}'$ lying on $\overline{A_1 A_2}$ can be computed from the linear system formed by the orthogonality conditions $(\mathbf{S}_{\mathrm{LIM}}')^{\mathrm{T}}[\overline{\nabla}\Omega(\mathbf{X}_{\mathrm{OPT}})] = 0$ and $(\mathbf{S}_{\mathrm{LIM}}'')^{\mathrm{T}}[\overline{\nabla}\Omega(\mathbf{X}_{\mathrm{OPT}})] = 0$.

Movements $\Delta x_i^{\lim}$ are resized as $\xi_i \Delta x_i^{\lim}$ $(i = 1, \ldots, N)$. Therefore, another set of random numbers ξ_i are defined in order to transform the limit directions into the descent directions $\mathbf{S}_{\mathrm{TR}}^q$ for which it holds $(\mathbf{S}_{\mathrm{TR}}^q)^{\mathrm{T}}[\overline{\nabla}\Omega(\mathbf{X}_{\mathrm{OPT}})] < 0$. It can be seen from Fig. 13 that the descent directions $\mathbf{S}_{\mathrm{TR}}^q$ are the diagonals of the search domain Σ – corresponding to the LKHM rectangle – while the last diagonal $\overline{P_{\mathrm{OPT}} L}$ is not a descent direction. The step size along the non-descent direction $\mathbf{S}_{\mathrm{ND}}$ is automatically set once step sizes on each descent direction have been defined. Say Δx_i^{ND} $(i = 1, \ldots, N)$ the movements defining the non-descent direction $\mathbf{S}_{\mathrm{ND}}$.

Each descent direction $\mathbf{S}_{\mathrm{TR}}^q$ is limited by the current optimum design P_{OPT} and a trial design $P_{\mathrm{TR}}^q(x_{\mathrm{OPT},1} + \Delta x_1^{q,\mathrm{fin}}, x_{\mathrm{OPT},2} + \Delta x_2^{q,\mathrm{fin}}, \ldots, x_{\mathrm{OPT},N} + \Delta x_N^{q,\mathrm{fin}})$, where the movements $\Delta x_i^{q,\mathrm{fin}}$ are determined by resizing movements $\Delta x_i^{\lim}$. These trial points are represented as circle dots in Fig. 13. A maximum of $(N + 1)$ descent directions are defined in order to limit the number of finite element analyses required in the characterization process. This strategy is "exact" in the case of isotropic hyper-elasticity where there are just the three (i.e., $N + 1$) directions $\mathbf{S}_{\mathrm{TR}}^1$, $\mathbf{S}_{\mathrm{TR}}^2$ and $\mathbf{S}_{\mathrm{TR}}^3$ (see Fig. 13). In the case of anisotropic hyper-elasticity, the additional N directions $\mathbf{S}_{\mathrm{TR}}^q$ are defined besides $\mathbf{S}_{\mathrm{TR}}^1$ by taking the most favourable combinations of increments $\sum_k[(\partial\Omega/\partial x_k) \cdot \Delta x_k]$, where $1 < k < N$. One starts with including in this sum $(N - 1)$ terms first, $(N - 2)$ terms then and progressively reduces the number of unknown components.

In order to refine the search locally, another set of trial points $P_{\mathrm{TR}}^{q,\mathrm{more}}(x_{\mathrm{OPT},1} + \eta_q \Delta x_1^{q,\mathrm{fin}}, x_{\mathrm{OPT},2} + \eta_q \Delta x_2^{q,\mathrm{fin}}, \ldots, x_{\mathrm{OPT},N} + \eta_q \Delta x_N^{q,\mathrm{fin}})$ are defined on the descent directions $\mathbf{S}_{\mathrm{TR}}^q$. For that purpose, a new set of random numbers η_q $(q = 1, \ldots, N + 1)$ are generated in the interval $(0, 1)$. These new trial points are indicated by triangular dots in Fig. 13.

Trial designs P_{TR}^q and $P_{\mathrm{TR}}^{q,\mathrm{more}}$ have been defined by perturbing simultaneously all optimization variables. This strategy is rather different from classical simulated annealing where design variables are perturbed one by one. For this reason, $2N$ additional trial designs are considered: $P_{\mathrm{TR}}^{i,1d}(x_{\mathrm{OPT},1}, x_{\mathrm{OPT},2}, \ldots, x_{\mathrm{OPT},i} + \Delta x_i, \ldots, x_{\mathrm{OPT},N})$ and $P_{\mathrm{TR}}^{i,1d,\mathrm{more}}(x_{\mathrm{OPT},1}, x_{\mathrm{OPT},2}, \ldots, x_{\mathrm{OPT},i} + \gamma_i \Delta x_i, \ldots, x_{\mathrm{OPT},N})$. These points, represented in Fig. 13 by cross-dots, are practically the components of the limit directions resized by means of the random numbers γ_i $(i = 1, \ldots, N)$. By doing this, the present SA algorithm considers populations of candidate designs much larger than the previous formulations developed by Lamberti and Pappalettere (2007) and Lamberti (2008), where there is only one candidate design for each descent direction $\mathbf{S}_{\mathrm{TR}}^q$. Remarkably, the present algorithm mixes "global" (i.e., perturbation of all design variables) and "1D" (i.e., perturbation of one variable at a time) information in order to find the best path towards the target optimum.

Fig. 13 shows that there are $2(N + 1) + 2N$ trial points that can potentially improve design. All of these trial points, within the Σ search domain, are stored in the Π_{GLOB} population. However, Σ will include also the "non-descent" point $P_{\mathrm{ND}}(x_{\mathrm{OPT},1} + \Delta x_1^{\mathrm{ND}}, x_{\mathrm{OPT},2} + \Delta x_2^{\mathrm{ND}}, \ldots, x_{\mathrm{OPT},N} + \Delta x_N^{\mathrm{ND}})$ lying on the non-descent direction $\mathbf{S}_{\mathrm{ND}}$. Another design $P_{\mathrm{ND}}^{\mathrm{more}}(x_{\mathrm{OPT},1} + v\Delta x_1^{\mathrm{ND}}, x_{\mathrm{OPT},2} + v\Delta x_2^{\mathrm{ND}}, \ldots, x_{\mathrm{OPT},N} + v\Delta x_N^{\mathrm{ND}})$ is hence generated by scaling movements Δx_i^{ND} with the v parameter defined as the smallest amongst the random numbers η_q and γ_i $(i, q = 1, \ldots, N)$ used for re-sizing step sizes along descent directions and in the 1D generation, respectively. The result of this operation is that the point $P_{\mathrm{ND}}^{\mathrm{more}}$ is closer to the current best record P_{OPT} than P_{ND} and eventual weight penalties might be reduced. However, since the Ω functional may be locally non-convex, there is no guarantee that the $P_{\mathrm{ND}}^{\mathrm{more}}$ design is better (i.e., less worse) than P_{ND}. For this reason, both P_{ND} and $P_{\mathrm{ND}}^{\mathrm{more}}$ points must be considered in the successive steps of the annealing process. The "non-descent" points P_{ND} and $P_{\mathrm{ND}}^{\mathrm{more}}$ are represented by square dots in the schematic of Fig. 13.

Step 3. Select the candidate design and evaluate its quality. Eventually use probabilistic criterion of acceptance/rejection.

The trial point $P_{\mathrm{TR}}(x_{\mathrm{TR},1}, x_{\mathrm{TR},2}, \ldots, x_{\mathrm{TR},N})$ for which there is the largest reduction in cost is selected from the Π_{GLOB} population as the best candidate design. Let $\Omega_{\mathrm{TR}}^{\mathrm{best}}$ denote the corresponding cost function value. The design $\mathbf{X}_{\mathrm{OPT}}$ found in each new optimization iteration is stored in the population of current best records Π_{OPT}. Let ITER be the number of iterations already completed before the current iteration. The database Π_{OPT} is comprised of $N \times$ ITER values assigned to the optimization variables and can be decomposed in N vectors each of which has ITER components. For instance, the vector $\mathbf{X}_{\mathrm{MEM}}^i$ includes the optimal values taken by the ith design variable in the past ITER iterations. If ITER > 2, for each design variable, one of these optimal values is randomly extracted from the corresponding vectors $\mathbf{X}_{\mathrm{MEM}}^i$ and stored then in the vector $\mathbf{X}_{\mathrm{OPT\text{-}MEM}}$. The corresponding value $\Omega_{\mathrm{OPT\text{-}MEM}}$ of the error functional Ω is computed in order to evaluate the quality of the current population Π_{GLOB} with respect to the development of the optimization process.

If $\Omega_{\mathrm{OPT\text{-}MEM}} < \Omega_{\mathrm{TR}}^{\mathrm{best}}$, accept the design $\mathbf{X}_{\mathrm{OPT\text{-}MEM}}$ as the new optimum $\mathbf{X}_{\mathrm{OPT}}$ and set $\Omega_{\mathrm{OPT}} = \Omega_{\mathrm{OPT\text{-}MEM}}$. Conversely, if $\Omega_{\mathrm{OPT\text{-}MEM}} > \Omega_{\mathrm{TR}}^{\mathrm{best}}$, accept the trial design $\mathbf{X}_{\mathrm{TR}}$ as the new optimum $\mathbf{X}_{\mathrm{OPT}}$ and set $\Omega_{\mathrm{OPT}} = \Omega_{\mathrm{TR}}^{\mathrm{best}}$. A new global annealing cycle is then performed by returning to Step 2.

If Π_{GLOB} does not include any points for which the error functional Ω can decrease, the acceptance probability value is computed for each "no-improvement" design $\mathbf{X}_{\mathrm{TR}}^s$ by using the Metropolis' probability function:

$$P(\Delta\Omega_{TR}) = \exp\left\{\frac{-\Delta\Omega_{TR}}{\left(\sum\limits_{r=1}^{NDW}\Delta\Omega_r/NDW\right)T_K}\right\} \tag{11}$$

where NDW is the number of trial points at which the cost function resulted larger than the current best records found throughout the optimization process. The $\Delta\Omega_r$ terms are the corresponding cost penalties. The ratio $\sum_{r=1,NDW}\Delta\Omega_r/NDW$ accounts for the general formation of all candidate designs previously generated and serves to normalize the probability function with respect to cost changes.

The generic trial design $\mathbf{X}_{TR}^s$ is provisionally accepted or certainly rejected according to the Metropolis' criterion re-formulated as

$$P(\Delta\Omega_{TR}^s) > \text{Max}[\rho_s, P(\Delta W_{ND}), P(\Delta W_{ND}^{more})] \Rightarrow \text{Provisionally accepted,}$$
$$P(\Delta\Omega_{TR}^s) < \text{Max}[\rho_s, P(\Delta W_{ND}), P(\Delta W_{ND}^{more})] \Rightarrow \text{Reject,} \tag{12}$$

where ρ_s is a random number in the interval $(0,1)$; $P(\Delta\Omega_{ND})$ and $P(\Delta\Omega_{ND}^{more})$ are the probability values computed for the cost function increments $\Delta\Omega_{ND}$ and $\Delta\Omega_{ND}^{more}$ corresponding to the points P_{ND} and P_{ND}^{more} defined on the non-descent direction $\mathbf{S}_{ND}$.

All trial designs provisionally accepted are stored in the population $\Pi_{GLOB}^{penalty}$. The trial point $\mathbf{X}_{TR}^{high\text{-}prob}$ with the highest value of acceptance probability is extracted from $\Pi_{GLOB}^{penalty}$ and set as the new current optimum design $\mathbf{X}_{OPT}$. The corresponding cost is set as the new best record: that is, $\Omega_{OPT} = \Omega_{TR}^{high\text{-}prob}$. The optimization process is restarted from Step 2.

If no trial design could be included in $\Pi_{GLOB}^{penalty}$, the classical 1D annealing search is performed by perturbing material parameters one by one (Step 4).

Step 4. Perform 1D annealing search.

If the global annealing search resulted unsuccessful, trial designs are generated in a random fashion by perturbing optimization variables one by one through M perturbation cycles. Therefore, $N \cdot M$ function evaluations are performed. The following scheme is utilized for generating random designs ($i = 1, \ldots, N$):

$$x_i = x_{OPT,i}^u + (\rho_i - 0.5)(x_i^u - x_i^l), \tag{13}$$

where ρ_i is a random number defined in the interval $(0,1)$ for the ith variable. The 0.5 threshold value serves to increase or reduce the current best value of the perturbed variable based on the magnitude of the random number generated.

By using Eq. (13), N new trial points $P_{TR,1d}^{local}(x_{OPT,1}, x_{OPT,2}, \ldots, x_i, \ldots, x_{OPT,N})$ are defined. These points are stored into the population Π_{LOC} which includes also the "1-directional" point $P_{TR}^{1d,max}$ selected from points $P_{TR}^{i,1d}$ and $P_{TR}^{i,1d,more}$ ($i = 1, \ldots, N$) previously defined with the global annealing search (Step 2). The point $P_{TR}^{1d,max}$ corresponds to the trial design with the highest value of acceptance probability evaluated by means of the criterion (12).

The trial point of the population Π_{LOC} yielding the largest reduction of the error functional Ω or possessing the highest acceptance probability again computed with Eq. (11) and evaluated with the acceptance/rejection criterion (12) is set as the new current best record. Once the $N \cdot M$ analyses required to perform the local annealing search have been completed, Step 5 can be executed.

Step 5. Check for convergence and eventually reset annealing parameters.

If $K > 3$, the SA-based code checks for convergence of the optimization process by using the following criterion:

$$\text{Max}\left\{\text{Max}\left[\frac{|\Omega_{OPT,K} - \Omega_{OPT,K-1}|}{\Omega_{OPT,K}}, \frac{|\Omega_{OPT,K-1} - \Omega_{OPT,K-2}|}{\Omega_{OPT,K-1}}, \frac{|\Omega_{OPT,K-2} - \Omega_{OPT,K-3}|}{\Omega_{OPT,K-2}}\right],\right.$$
$$\left.\text{Max}\left[\frac{||X_{OPT,K} - X_{OPT,K-1}||}{||X_{OPT,K}||}, \frac{||X_{OPT,K-1} - X_{OPT,K-2}||}{||X_{OPT,K-1}||}, \frac{||X_{OPT,K-2} - X_{OPT,K-3}||}{||X_{OPT,K-2}||}\right]\right\} \leqslant \varepsilon_{CONV} \tag{14}$$

where $\Omega_{OPT,K}$ and $\mathbf{X}_{OPT,K}$, respectively, denote the best record and the corresponding design vector found in the Kth cooling cycle. The parameter ε_{CONV} is set to 10^{-10}. If the convergence criterion is satisfied, the optimization process is terminated and Step 6 is executed.

If $K < 3$ or the convergence criterion (14) remains unsatisfied, the K counter of annealing cycles is reset as $K = K + 1$. Temperature is then reduced in fashion of $T_{K+1} = \beta_K T_K$. The parameter β_K is computed as

$$\beta_K = \left[\sum_{r=0}^{K-1}\beta_r/K\right]\text{Max}\left[\frac{0.95}{\left(1 + \frac{N_{REJE}}{N_{TRIA}}\right)}, \left(1 - \frac{\Omega_{FIN,K-1}}{\Omega_{INIT,K-1}}\right)\right], \tag{15}$$

where $\Omega_{FIN,K-1}$ and $\Omega_{INIT,K-1}$, respectively, are the error functional values at the beginning and at the end of the current annealing cycle. N_{REJE} is the number of trial designs rejected out of the total number of trial designs N_{TRIA} generated in the current cooling cycle; N_{REJE} includes each trial point which did not yield immediate improvement in design. The correction term $[\sum_{r=0}^{K-1}\beta_r/K]$ is the average of all of the β_K factors defined in the optimization process until the current annealing cycle is being executed. As is clear, the correction term is equal to 1 in the first annealing cycle.

The optimization process is restarted from Step 2.

Step 6. End the optimization process and store optimization results.

2.7. Implementation details

The SA-based optimization algorithm described in the preceding section can be easily integrated into a commercial finite element package. Therefore, the optimization routine has been coded in the own programming language of the ANSYS software. There is a main code denoted as *ANNEAL* and a routine code denoted as *ANALYSIS*.

The main code *ANNEAL* reads input data (i.e., displacement target values measured experimentally, initial values of material properties and their corresponding side constraints, convergence tolerance, cooling parameters, number of annealing cycles to be performed, etc.), includes loops for perturbing randomly all material parameters simultaneously or one at a time, stores trial designs in the corresponding populations and handles output quantities.

The *ANALYSIS* routine, called by the main code *ANNEAL*, calculates the new structural response each time the material properties are perturbed and a new trial design is generated thus updating the error functional Ω. Computations then return back to the *ANNEAL* main code level. The current value of Ω is compared with the current best solution stored in the optimization process and the new search strategy is hence decided according to Steps 2–5.

All operations listed in the main code *ANNEAL* are executed at the /BEGIN level of the ANSYS software. Model updating, assignment of material parameters, specification of loading and constraint conditions are done at the/PREP7 level. Structural analysis and evaluation of the error functional Ω are, respectively, executed at the/SOLUTION and/POST1 levels.

Structural analysis and optimization runs entailed by the characterization process have been carried out on a standard PC equipped by a 3.4 GHz Intel Pentium® Dual Core processor with 4 Gb of RAM memory. One structural analysis took about 30 s for the natural rubber specimen and about 250 s for the bovine pericardium patch. The entire optimization process has been completed, respectively, within about 2.5 and 10 h of wall-clock time. The annealing process always required less than 500 structural analyses for the rubber membrane and less than 2000 structural analyses for the pericardium patch. Remarkably, the number of analyses performed in the anisotropic case is only 4 times larger than for the isotropic case although the number of design variables considered for the pericardium patch is more than 8 times larger than for the rubber specimen (i.e., 17 vs. 2). This fact confirms the efficiency of the proposed SA algorithm and the importance of using largely sized populations of candidate designs.

3. Results and discussion

Table 1 summarizes the results obtained for the isotropic hyper-elastic membrane made of natural rubber. Data are relative to the maximum pressure of 15.25 kPa. The table lists the initial values assigned to Mooney–Rivlin constants and the corresponding values obtained with the optimization-based identification process. Percent errors on material properties with respect to target values independently determined with the planar biaxial calibration tests are also shown in the table. It can be seen that the largest error on hyper-elastic constants is always less than 1.5% in all optimization runs. Errors increased when u-displacements are included as target quantity in the error functional Ω. Remarkably, optimization results are insensitive to starting point. In fact, standard deviations of a_{10} and a_{01} with respect to target values are only 0.51% and 0.63%, respectively.

Values of residual errors on displacements are also listed in Table 1. The average error is always less than 2.3%. The largest error overall is less than 3.6%. Matching u-displacements resulted in slightly larger errors than matching w-displacements or

Table 1
Natural rubber membrane: results of the characterization process for different optimization runs

Initial guess on MR constants	Displacement components matched	MR constants (kPa)	Percent error on MR constants (%)	Percent error on displacements (%)
$a_{10} = 80$ kPa; $a_{01} = 1$ kPa	u	$a_{10} = 203.643$	1.304	Average 2.231
		$a_{01} = 13.376$	1.318	Largest 3.597
	w	$a_{10} = 201.344$	0.160	Average 1.515
		$a_{01} = 13.353$	1.144	Largest 2.989
	u_{tot}	$a_{10} = 201.318$	0.147	Average 1.542
		$a_{01} = 13.354$	1.151	Largest 3.293
$a_{10} = 1$ MPa; $a_{01} = 20$ kPa	u	$a_{10} = 203.229$	1.098	Average 2.213
		$a_{01} = 13.398$	1.485	Largest 3.533
	w	$a_{10} = 202.403$	0.687	Average 1.543
		$a_{01} = 13.336$	1.015	Largest 3.404
	u_{tot}	$a_{10} = 203.244$	1.105	Average 1.602
		$a_{01} = 13.166$	0.273	Largest 3.487

Target values of Mooney–Rivlin constants are $a_{10} = 201.022$ kPa and $a_{01} = 13.202$ kPa.
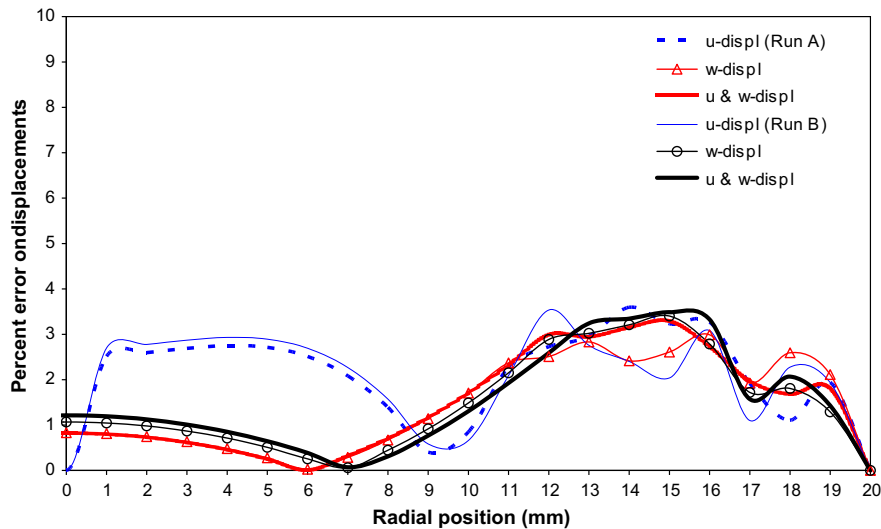
Fig. 14. Natural rubber membrane. Distribution of residual error on displacements for the different optimization runs.

global displacements. This fact can be explained with the informal argument that u-displacements are smaller in magnitude and hence may be more sensitive to small variations of hyper-elastic constants.

Fig. 14 shows the residual errors evaluated at control nodes for the different optimization runs. As expected, error values are maximum near membrane boundaries for each displacement component considered in the optimization process. This could be because the O-ring seal fixture did not realize the perfect clamping hypothesized in the finite element model. Residual errors on u-displacements increase near the centre of the membrane. Again, this behaviour could be due to the fact that u-displacements are very small in magnitude near the pole of the inflated membrane.

Fig. 15 compares the displacement values expressed in the "moiré" reference system and their counterpart expressed in the global reference system. The plot shown in the top of the figure is relative to Run B executed by considering the out-of-plane displacement w as target quantity. As expected, finite element predictions matched much more accurately the displacement values expressed in the global reference system. In particular, deviations became much larger near membrane boundaries. This is because the curvature of deformed surface increases as one moves away from the central region of the membrane. However, as the curvature increases, the plane tangent to the surface of the membrane representing the "moiré" reference system to which fringe patterns are referred becomes more inclined with respect to the image plane which is instead lined up with the global reference system. This misalignment may result in significant errors on in-plane displacements and consequently affects also the final value of the out-of-plane component.

The plot in the bottom of the figure is instead relative to the optimization run carried out including the total displacement u_{tot} as target quantity. Again, errors are very large (up to 21%) near membrane boundaries if displacement components are expressed in the "moiré" reference system.

Table 2 reports the results obtained in two additional optimization runs carried out by including as target quantities in the Ω functional the displacement values expressed in the local reference system. Initial values of MR constants correspond to Run B. It can be seen that matching FE predictions with "local" displacements led to wrong results. In particular, the error on a_{01} raised to more than 50%. The error on a_{10} is also significant: between 2 and 5 times larger than for the "global" reference system case. The average error on displacements is more than twice larger than in the "global" reference system case while the largest error on displacements raised to about 25%.

The analysis of residual error distributions plotted in Fig. 16 reveals that using target displacement values referred to the "moiré" reference system led to increase dramatically errors in the critical regions (i.e., near the membrane pole and boundaries). Although in one case the "local" reference system optimization seems to produce results good enough (the error on MR constants is less than 2.5%: $a_{10} = 196.285$ kPa and $a_{01} = 12.876$ kPa vs., respectively, 201.022 and 13.202 kPa), the displacement values predicted by a finite element analysis carried out including $a_{10} = 196.285$ kPa and $a_{01} = 12.876$ kPa as material properties are much more consistent (average error is 2.726% vs. 5.290%) with the displacement values expressed in the global reference system than with the target "moiré" values with respect to which the optimization run was performed.

Fig. 17 shows the SA convergence curves for the natural rubber membrane. The number of annealing cycles completed in the matching process is rather insensitive to the initial values hypothesized for material properties. As is clear, the final value of the cost functional Ω depends on the specific combination of target displacements considered in the optimization. Furthermore, the speed of the optimization process does not change much if displacement values expressed in the "moiré" reference system are taken as target quantity. Apart from the obvious differences in the value of cost function Ω caused by the
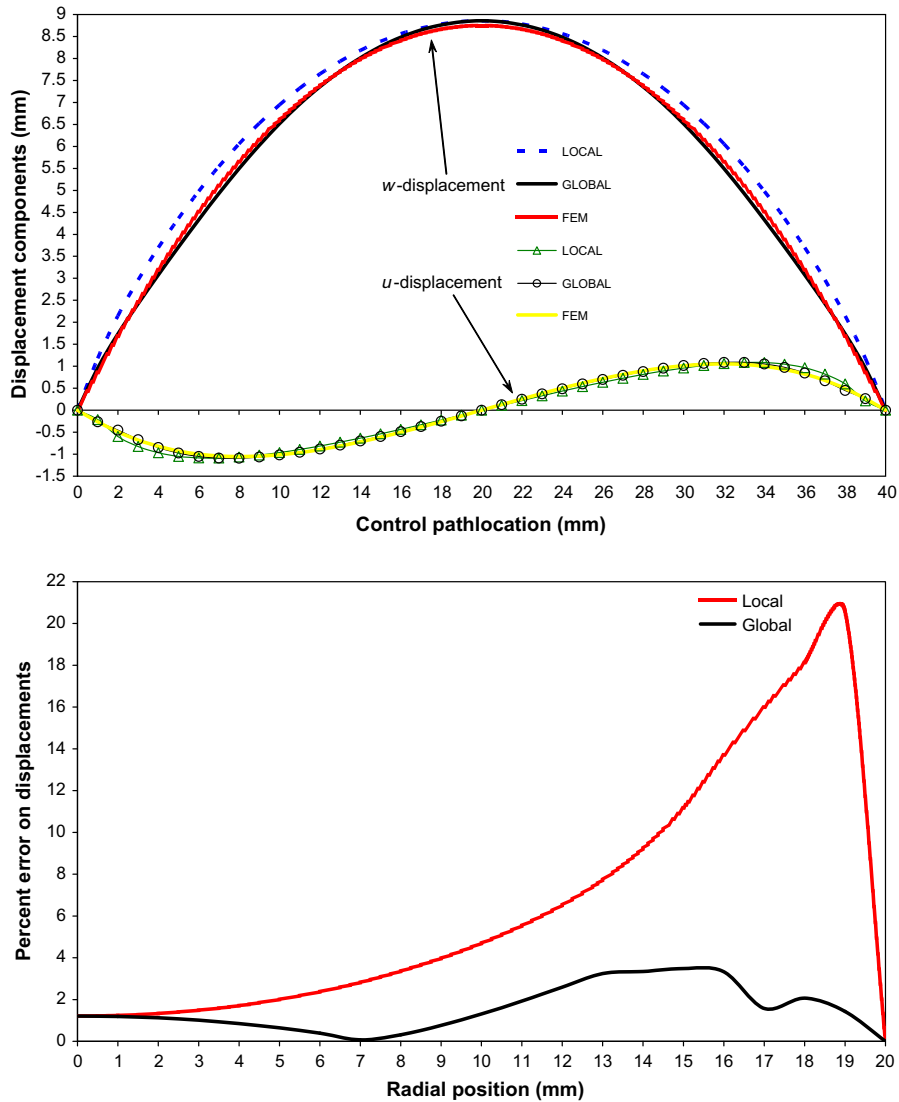
Fig. 15. Natural rubber membrane. Comparison of experimentally measured displacements and finite element predictions after the optimization process.

Table 2
Natural rubber membrane: comparison of "LRS" and "GRS" optimization results

Initial guess on MR constants	Reference system	Displacement components matched	MR constants (kPa)	Error on MR constants (%)	Error on displacements (%)
$a_{10} = 1$ MPa; $a_{01} = 20$ kPa	GLOBAL	u	$a_{10} = 203.229$	1.098	Average 2.213
			$a_{01} = 13.398$	1.485	Largest 3.533
		u_{tot}	$a_{10} = 203.244$	1.105	Average 1.602
			$a_{01} = 13.166$	0.273	Largest 3.487
	LOCAL "Moiré"	u	$a_{10} = 212.298$	5.609	Average 11.962
			$a_{01} = 6.525$	50.576	Largest 21.569
		u_{tot}	$a_{10} = 196.285$	2.413	Average 5.920
			$a_{01} = 12.876$	2.469	Largest 24.493

large errors made in the "local" reference system optimization, the number of annealing cycles required to approach the point of minimum for Ω does not change significantly. These facts confirm with no shadow of doubt the robustness of the SA-based optimizer utilized in this research.
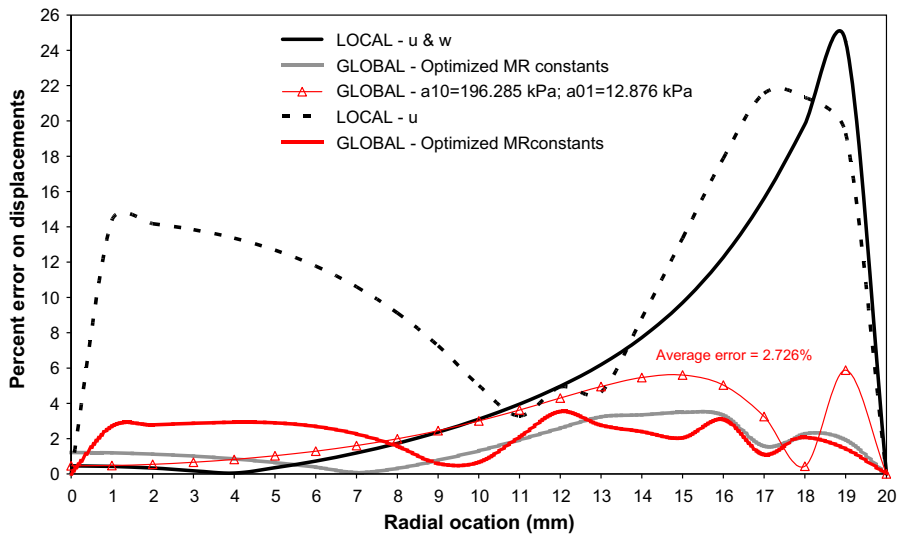
Fig. 16. Natural rubber membrane. Optimization results obtained by including "local" displacements in the error functional Ω.
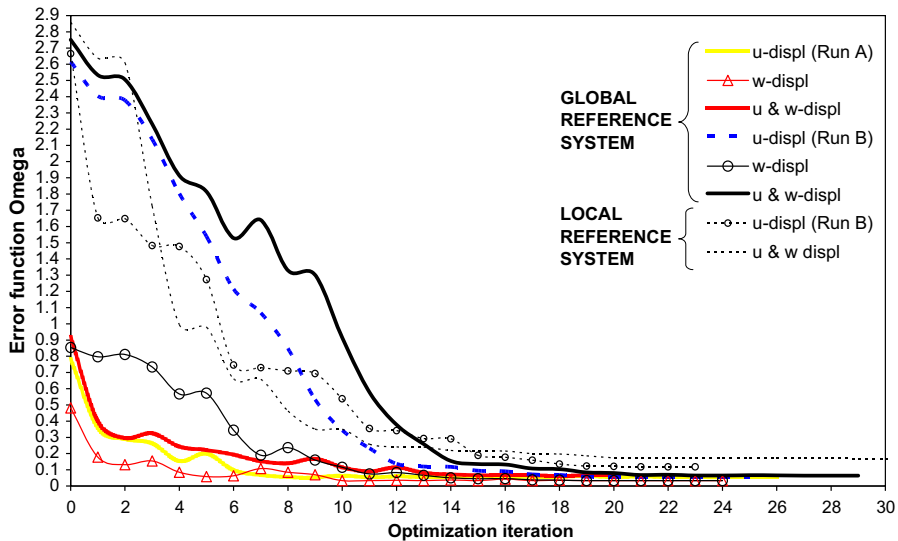

Fig. 17. Natural rubber membrane. Convergence curves for different optimization runs carried out in the identification process.

Table 3 reports the results obtained for the bovine pericardium patch; data are relative to the maximum pressure of 12.22 kPa. It can be seen that the SA-based optimizer found also in this case material properties very close to the target values. In fact, the average error on hyper-elastic constants and fibre orientation is less than 1% (i.e., 0.550% and 0.975% for Runs A and B, respectively) and the corresponding standard deviation is 1.085%. The largest difference with respect to the target properties determined with the planar-biaxial test conducted in the calibration phase is, respectively, 1.621% (i.e., for constant b_3) in Run A and 3.677% (i.e., for constant d_3) in Run B. Remarkably, the difference on hyper-elastic constants exceeded 1.5% only in other three cases (i.e., a_3, b_2 and d_5). Percent differences on material properties with respect to target values resulting from optimizations Runs A and B are distributed in a fairly random fashion. This fact leads to conclude that the SA-based routine always converged globally to the same target design and there was no specific material parameter driving the optimization process.

It can be seen from Table 3 that the average residual error on total displacements is 1.5% (i.e., 1.505% and 1.493% for Runs A and B, respectively) while the corresponding maximum error is about 3% (i.e., 2.941% and 3.008% for Runs A and B, respectively). Distributions of residual errors on u_{tot} displacements evaluated along the two control paths h_c and v_c considered in the identification process are plotted in Fig. 18. Error trends are similar to those observed in the case of the isotropic rubber membrane: errors increase sharply in the region where in-plane displacements are largest and near membrane boundaries.

Table 3
Bovine pericardium patch. Results of the identification process for different optimization runs

Material properties	GLOBAL – Run A	GLOBAL – Run B	LOCAL (Cosola et al., 2008)
a_1	199.270	199.137	199.357
a_2	125.717	126.278	126.334
a_3	135.071	137.162	135.041
b_1	386.253	390.180	387.799
b_2	170.630	166.608	170.465
b_3	189.082	186.201	186.066
c_2	199.099	195.633	197.786
c_3	89.390	88.712	89.976
c_4	174.704	173.544	174.898
c_5	169.737	169.516	169.682
c_6	147.190	149.012	148.472
d_2	158.352	159.242	158.028
d_3	21.227	22.192	21.405
d_4	68.651	69.431	69.605
d_5	167.888	170.563	165.645
d_6	102.371	102.090	101.767
$\cos\theta_f$	0.6833	0.6846	0.6833
Error on material properties (%)	Average 0.550 Largest 1.621	Average 0.975 Largest 3.677	
Error on displacements (%)	Average 1.505 Largest 2.941	Average 1.493 Largest 3.000	

The hyper elastic constants a_i, b_j, c_k and d_l are expressed in kPa.
Initial designs: $a_i = b_j = c_k = d_l = 10$ kPa, $\cos\theta_f = 0.7$ for Run A; $a_i = b_j = c_k = d_l = 1$ MPa, $\cos\theta_f = 0.7$ for Run B.
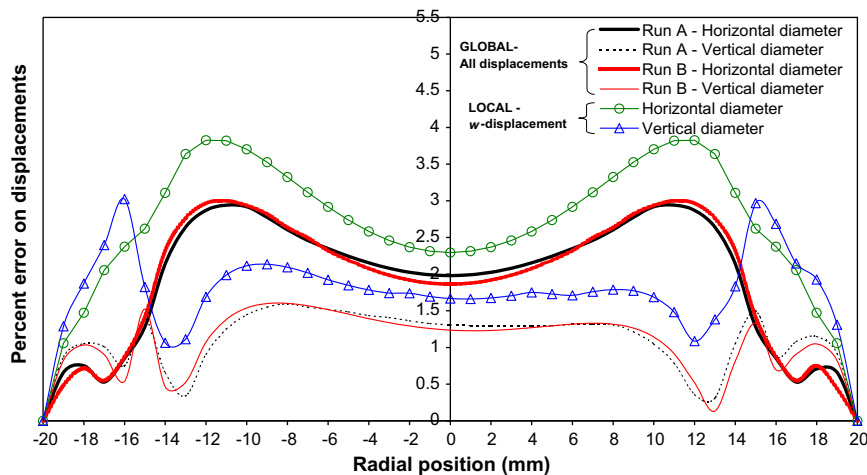

Fig. 18. Bovine pericardium patch. Comparison of experimentally measured displacements and finite element predictions after the optimization process.

However, material anisotropy resulted in different error distributions along the horizontal and vertical control paths and yield some asymmetry in the error plots; edge effects are more pronounced for the Y-direction.

The identification process of the pericardium patch confirmed the need for having displacements expressed in the global reference system. Table 4 compares the residual errors on displacements made in Runs A and B with those relative to the calibration campaign (Cosola et al., 2008). As explained in Section 2.5, the results of the planar equi-biaxial test carried out on the pericardium patch were verified by giving the target material properties determined via optimization in input to a finite element model simulating another inflation test carried out independently. However, out-of-plane displacements measured experimentally with projection moiré were compared with finite element predictions without accounting for the presence of the in-plane displacements in the inflation test and, consequently, not accounting for membrane curvature changes with respect to the image plane. Therefore, the locations in the image plane corresponding to control points were referred to the "local" reference system of the moiré grating printed on the deformed surface (see discussion in Section 2.1). It can be seen from Table 4 that the average error on displacements became about 50% larger for the horizontal control path h_c and about two times larger for the vertical control path v_c if the local reference system is considered. The same behaviour was observed for the maximum error.

Table 4
Bovine pericardium patch: sensitivity of optimization results to the reference system considered in the identification process

Reference system	Average error on displacements (%)	Maximum error on displacements (%)
GLOBAL – Run A All displacements	Control path h_c 1.914 Control path v_c 1.095	Control path h_c 2.941 Control path v_c 1.594
GLOBAL – Run B All displacements	Control path h_c 1.916 Control path v_c 1.071	Control path h_c 3.000 Control path v_c 1.602
LOCAL w-displacement (Cosola et al., 2008)	Control path h_c 2.777 Control path v_c 1.823	Control path h_c 3.826 Control path v_c 3.023

Further evidence can be gathered from Fig. 18 where error distributions relative to the local reference system case are also plotted. It can be seen that while the error magnitude near the membrane pole are comparable regardless of the chosen reference system, errors sharply increase in the region where in-plane displacements are largest and have more or less the same magnitude of out-of-plane displacements. This behaviour is consistent with that observed for the isotropic rubber membrane. Therefore, the composition of displacement components becomes strictly necessary if all displacement components are of the same order of magnitude and hence contribute significantly in the resulting global displacement vector.

Fig. 19 shows that the convergence speed of the SA-based routine is again insensitive to the initial values assigned to material properties. The optimization process carried out for the GTBP patch has been completed in 35 and 34 annealing cycles, respectively, for Run A and B. However, the corresponding convergence curves practically coincided after only 25 iterations and the error functional Ω did not change significantly till the end of the optimization process. The robustness of the SA-based routine presented in this paper is confirmed by the fact that the number of annealing cycles changed slightly with respect to the case of the isotropic rubber membrane although the identification problem of the pericardium patch included 17 variables vs. only 2 of the isotropic material. Furthermore, Run B started from a design vector about 840% different from the target material properties while this difference was only 226% in the case of the rubber membrane. Indeed, the very large number of design variables included in the identification problem of the bovine pericardium patch as well as the multi-point annealing strategy contributed to increase very much the size of the population of candidate designs considered in the simulated annealing process thus expanding the portion of design space explored in the optimization process. This allowed convergence speed to be significantly enhanced in the more complicated identification problem.

Convergence behaviour seems to improve when all of the displacement components are included in the optimization. This is because out-of-plane displacements are much larger in magnitude than in-plane displacements and therefore drive the search process. In order to support this statement, one can observe that the error functional Ω decreased in Runs A and B much more quickly than for the SA-based optimization carried out in the calibration campaign where the in-plane displacements were included as target quantity in the Ω functional (Cosola et al., 2008). This occurred in spite of the fact that in the 3D moiré setup case the difference between initial and target designs was between 4 and 14 times larger than for the 2D moiré setup used in the calibration campaign (i.e., about 226 or 840% vs. about 58%). As is clear, numerical noises occurred
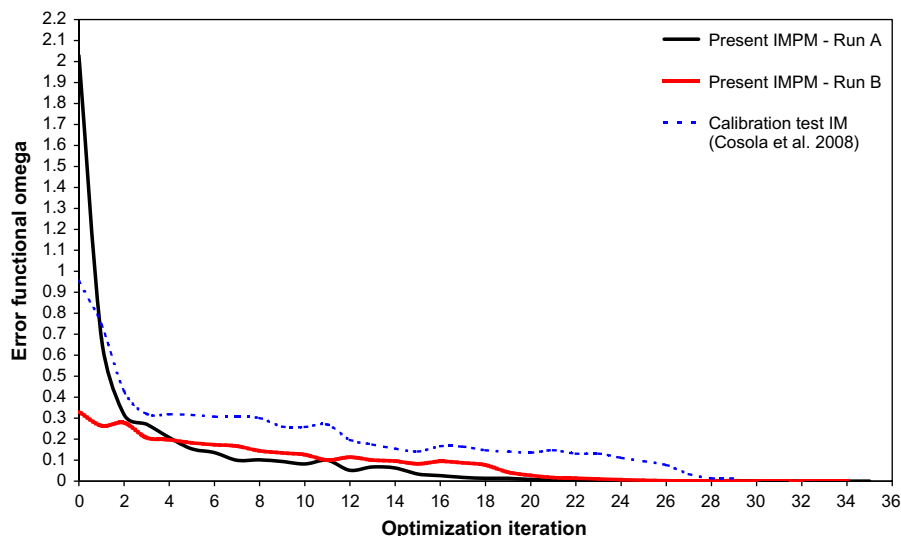
Fig. 19. Bovine pericardium patch. Convergence curves for different optimization runs carried out in the identification process.

for the very small in-plane displacements, but not for the large out-of-plane displacements, and resulted in marginal improvements in cost for many annealing cycles.

Finally, the sensitivity of optimized designs to perturbations of material properties has been also analysed. For that purpose, all optimized values of hyper-elastic constants and fibre orientation have been reduced or increased by 10% and new finite element analyses have been executed in order to re-compute distributions of residual errors on displacements. The response of the isotropic rubber membrane is much more sensitive to perturbations of material properties than the response of the anisotropic GTBP patch. In fact, while the error magnitude never went above 4.35% for the pericardium patch, the average error raised to more than 10% even for a 10% variation of a_{10} in the case of the isotropic rubber membrane. This occurred in spite of the fact that values of average residual errors on displacements were comparable for all optimized designs (see Tables 1 and 3). However, the observed behaviour was somehow expected and can be explained rather easily with the larger amount of design freedom introduced in the GTBP patch case by the 17 unknown material parameters included as optimization variables.

Fig. 20 shows the error plots relative to the sensitivity analysis carried out for the pericardium patch. The 10% increment or the 10% reduction in material parameters are, respectively, indicated in the plots by the (+) and (−) notations. It can be seen that the largest error magnitude is 4.35% or 2.90%, respectively, for the horizontal (Fig. 20a) and vertical (Fig. 20b) control paths. Results of sensitivity analysis are somehow similar for both materials: in fact, the solution is rather sensitive to coefficients a_i and b_j of the isotropic deviatoric term $W_{d,iso}$ (i.e., that accounting for the matrix behaviour) of the strain energy
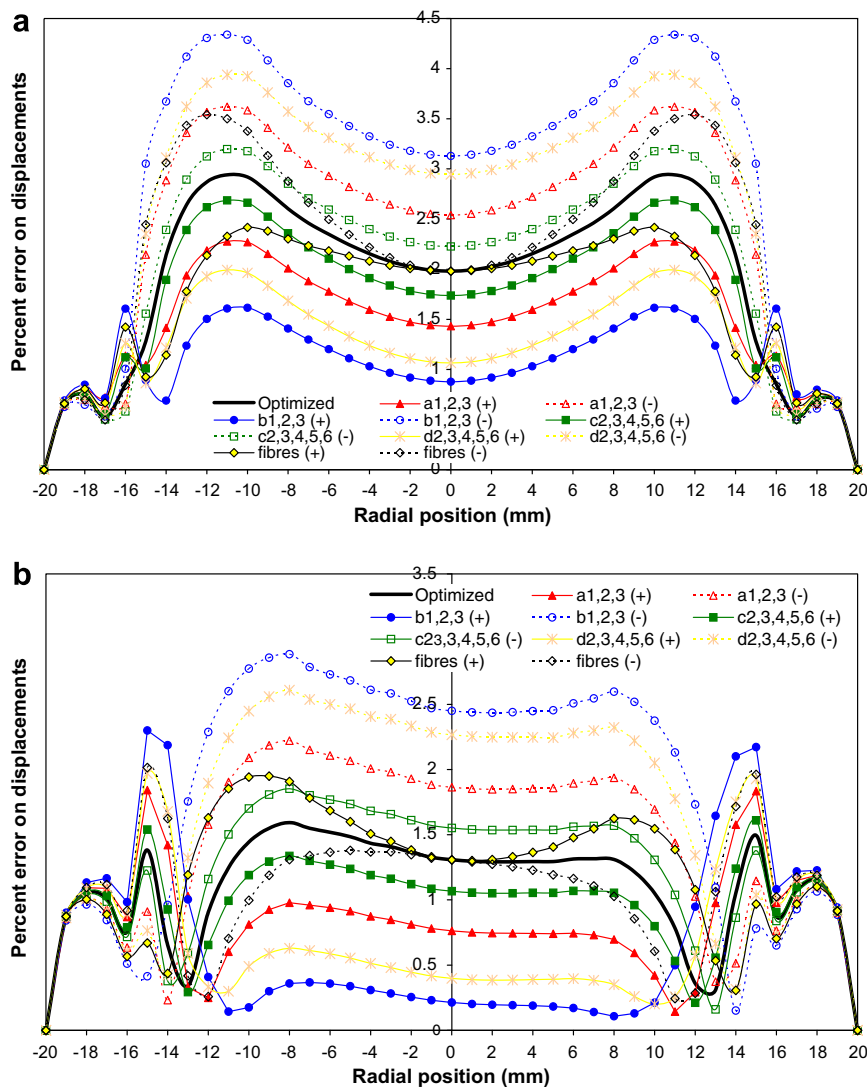

Fig. 20. Bovine pericardium patch. Sensitivity of residual errors on displacements to perturbations of optimized material properties: (a) horizontal diameter and (b) vertical diameter.

function in Eq. (6). The average error on displacements became smaller than for the optimized designs if hyper-elastic constants b_1, b_2, b_3 or d_2, d_3, d_4, d_5, d_6 are increased by 10%. However, this would have resulted in rather large errors in the region where in-plane displacements are comparable with out-of-plane displacements (see the local peaks in the residual error distributions plotted in Fig. 20). As is clear, this would have complicated the process of convergence of the SA-based optimization routine. Sensitivity analysis hence confirmed once again the necessity of including all displacement components in the error functional Ω. In fact, the structural response of a thin hyper-elastic membrane is very sensitive to changes in material properties just in the regions where in-plane displacements are comparable in magnitude with out-of-plane displacements. If displacements were expressed in the local reference system (i.e., the "moiré" system) without accounting properly for their mutual interaction in composing the global displacement vector, large residual errors and hence high values of the error functional Ω might have occurred in the identification process even for small oscillations in material property values.

4. Concluding remarks

This paper presented a framework for mechanical characterization of hyper-elastic materials. The hybrid procedure utilized moiré techniques, finite element analysis and multi-point simulated annealing optimization. A novel experimental set-up based on a proper combination of intrinsic and projection moiré allowed the 3D displacement components to be simultaneously and independently measured with the same experimental setup and just one camera. The very common approach followed in literature where only one displacement component measured optically is taken as target quantity has hence been made absolutely general in this research.

The efficiency of the new framework presented in the paper was tested in the mechanical characterization of two different hyper-elastic materials: (i) an isotropic membrane made of natural rubber following the two constant Mooney–Rivlin constitutive law; (ii) an anisotropic GTBP patch modelled as a transversely isotropic material. In the latter case, the number of material parameters to be identified raised to 17. The inflation test was chosen as the only experimental protocol utilized in the characterization process.

Remarkably, the MR constants determined at the end of the characterization process of the natural rubber membrane were in excellent agreement with target values found independently: less than 1% difference. The same happened also for the anisotropic bovine pericardium patch: in fact, the maximum error on material parameters was about 3.5%.

In the case of the rubber membrane, the residual error on displacements evaluated in correspondence of the MR constants that minimized the error functional Ω was less than 3.5%. Although it might be surprising that the residual percent error on displacement is more than three times as large as the percent error on hyper-elastic constants, one has to remind that the structural response of an inflated hyper-elastic membrane is highly non-linear. However, the above-mentioned discrepancy became less significant for the bovine pericardium patch: in fact, the largest error on displacements was about 3% vs. about 3.5% error on hyper-elastic constants. Such a behaviour can be explained with the informal argument that the considerably large number of material parameters included in the GTBP constitutive model makes the error functional Ω to be overall less sensitive to even fairly large errors on some specific hyper-elastic constant. In simple words, the error functional Ω is affected at different extents by the errors made on the different material properties. Therefore, even a "rather large" error on some hyper-elastic constant does not necessarily imply large residual errors on displacements.

The results obtained in this study demonstrate with no shadow of doubt the feasibility and robustness of the proposed approach which worked very well for both isotropic and anisotropic hyper-elasticity. Since all displacement components were simultaneously measured using the same experimental setup and hence compared with FE predictions provided by a single numerical model, thus avoiding the obvious complications entailed by setting up different test protocols and simulating each experimental test with the same degree of accuracy and reliability, the present framework for mechanical characterization of hyper-elastic materials seems to be very general and should be utilized in all those cases where it is not possible to realize uniform strain/stress states.

Besides the novelty in having introduced only one experimental setup for simultaneously measuring all displacement components, the importance of having a powerful optimization routine inherently able to deal with non-linearity and non-convexity entailed by the identification problem has been clearly underlined in the paper. The present simulated annealing formulation is certainly a state-of-the-art optimization algorithm and is truly innovative in the sense that populations of candidate designs each of which has a real probability of reducing the error functional Ω are generated in each annealing cycle. Furthermore, the SA algorithm keeps memory of the different best records progressively generated in the search process. Finally, the SA code is highly flexible because can change search strategy based on the current development of the optimization process. Remarkably, the simulated annealing algorithm utilized in this paper allowed the search process to be completed within the same optimization run. The commercial finite element code ANSYS required instead multiple-start gradient based optimization runs and much more iteration cycles: for example, after 30 iterations, the error functional Ω was still greater than 0.55 and 0.25, respectively for Run A and Run B, while the SA routine already converged practically to the final design.

From the previous discussion, it can be stated that the hybrid identification procedure presented in this research represents an important step further with respect to other hybrid procedures – like, for instance, those presented by the last three authors (Genovese et al., 2005, 2006) – where only one displacement component was considered as target quantity because of constraints on the complexity of experimental setups. However, the "one displacement component" approach can work

well for "rather simple" constitutive laws but might fail for more complicated constitutive behaviours. The larger amount of information made available by the present approach, with no extra cost in terms of experimental setup complexity, improved significantly the entire characterization procedure which was able to deal successfully even with a real biological membrane following a complicated constitutive law such as transversely isotropic hyper-elasticity.

The achievements reached in this research are relevant. In fact, although many sophisticated hyper-elastic models have recently been presented in literature (see, for instance, Attard and Hunt, 2004; Itskov and Aksel, 2004; Limbert and Middleton, 2004; Sun and Sacks, 2005; Guo et al., 2006; Holzapfel, 2006; Balzani et al., 2006; Drozdov, 2007; Massabò and Gambarotta, 2007), the validation of these formulations often relies on the assumption of homogeneous strain states which may hardly be reproduced through experimental tests or is limited to simple loading cases such as uniform axial tension or compression or pure shear. The present approach overcomes this limitation because it deals simultaneously with all displacement components without making any assumption on loading and constraint conditions. This conclusion is supported by the excellent results obtained for both isotropic hyper-elastic materials (i.e., natural rubber) and for real anisotropic biological membranes (i.e., bovine pericardium patch).

The existence of analytical solutions for identification problems in anisotropic hyper-elasticity is a very debated question because of the huge mathematical complexity which does not allow us to employ the straightforward material property fitting procedures available for isotropic hyper-elastic materials. Constitutive behaviour of anisotropic materials identified via hybrid procedures should always be validated by carrying out other independent tests. This requirement was certainly satisfied in the present research since material properties identified via optimization of 3D data obtained from an inflation test matched very well the corresponding values obtained in the calibration phase from 2D data gathered with a planar equibiaxial test.

Although the present identification process could be used as a black-box, some facts should be carefully considered. In the first place, moiré patterns have to be transformed into displacement information expressed in the global reference system. This question becomes more and more important as the distortion experienced by the specimen is larger.

Second, it may be difficult to realize the conditions of projection and viewing from infinity. This fact could suggest the use of photogrammetry and multi-camera systems for contouring out-of-plane displacements (see, for instance, Grytten et al., 2007). The error made on the out-of-plane displacement value for a given point P of the deformed surface corresponds to the error made on a spatial coordinate equal to the distance between P and the reference plane. The figure generally accepted for quantifying maximum accuracy on spatial coordinates measured with photogrammetry is 10^{-5} of the largest dimension of the analyzed object. However, PM has been proven to be substantially competitive with photogrammetry regardless of the size of the investigated object (see, for instance, Sciammarella et al., 2005; Galietti et al., 2007; Sciammarella et al., 2008a,b,c). This was achieved by implementing correction functions very simple compared to the complicated bundle adjustment software which is usually utilized in photogrammetry. Furthermore, the condition of projection from infinity can be realized rather easily through interference of two identical gratings projected by point sources located symmetrically about the optical axis of the camera.

The last issue is the level of accuracy reached in the moiré measurements. This is very important in view of the fact that structural response may be sensitive to even very little perturbations of material properties especially in those regions where displacement magnitude is small. Therefore, the standard deviation of measured displacements with respect to target values may become a critical quantity. Based on the considerable amount of experimental data available from the above mentioned studies on moiré and considering the present values of sensitivity, the standard deviation of displacement values measured with the IMPM setup developed in this paper can be estimated as about 6 μm. This is a very small quantity compared to displacement values (between 500 and 8850 μm) that were measured in the present experiments and therefore does not affect at all the validity of the results obtained in this research.

References

ANSYS® Version 10.0, 2007. Theory and User's Manual. ANSYS Inc., Canonsburg, PA, USA.
Attard, M.M., Hunt, G.W., 2004. Hyperelastic constitutive modeling under finite strain. International Journal of Solids and Structures 41, 5327–5350.
Avril, S., Pierron, F., 2007. General framework for the identification of constitutive parameters from full-field measurements in linear elasticity. International Journal of Solids and Structures 44, 4978–5002.
Balzani, D., Neff, P., Schröder, J., Holzapfel, G.A., 2006. A polyconvex framework for soft biological tissues. Adjustment to experimental data. International Journal of Solids and Structures 43, 6062–6070.
Cloud, G.L., 1998. Optical Methods of Engineering Analysis. Cambridge University Press, New York, USA.
Cosola, E., Genovese, K., Lamberti, L., Pappalettere, C., 2008. Mechanical characterization of biological membranes with moiré techniques and multi-point simulated annealing. Experimental Mechanics 48, 465–478.

Cugnoni, J., Gmur, T., Schorderet, A., 2007. Inverse method based on modal analysis for characterizing the constitutive properties of thick composite plates. Computers and Structures 85, 1310–1320.

Cunha, J., Cogan, S., Berthod, C., 1999. Application of genetic algorithms for the identification of elastic constants of composite materials from dynamic tests. International Journal for Numerical Methods in Engineering 45, 891–900.

Drozdov, A.D., 2007. Constitutive equations in finite elasticity of rubbers. International Journal of Solids and Structures 44, 272–297.

Freed, A.D., Einstein, D.R., Vesely, I., 2005. Invariant formulation for dispersed transverse isotropy in aortic heart valves. An efficient means for modeling fiber splay. Biomechanics and Modeling in Mechanobiology 4, 100–117.

Fung, Y.C., 1993. Biomechanics Mechanical Properties of Living Tissues, second ed. Springer, New York.

Galietti, U., Genovese, K., Lamberti, L., Posa, D., 2007. A simple Projection Moiré System to measure displacements of aircraft structures. Journal of Strain Analysis for Engineering Design 42, 477–495.

General Stress Optics Inc., 2008. Holo-Moiré Strain Analyzer software HoloStrain™, Version 2.0. Chicago, IL, USA. Available from: <www.stressoptics.com>.

Genovese, K., Lamberti, L., Pappalettere, C., 2005. Improved global-local simulated annealing formulation for solving non-smooth engineering optimization problems. International Journal of Solids and Structures 42, 203–237.

Genovese, K., Lamberti, L., Pappalettere, C., 2006. Mechanical characterization of hyperelastic materials with fringe projection and optimization techniques. Optics and Lasers in Engineering 44, 423–442.

Goldberg, D.E., 1989. Genetic Algorithms in Search, Operation and Machine Learning. Addison-Wesley, Reading, MA.

Grytten, F., Fagerholt, E., Auestad, T., Forre, B., Borvik, T., 2007. Out-of-plane deformation measurements of an aluminium plate during quasi-static perforation using structured light and close-range photogrammetry. International Journal of Solids and Structures 44, 5752–5773.

Guo, Z.Y., Peng, X.Q., Moran, B., 2006. A composites-based hyperelastic constitutive model for soft tissue with application to the human annulus fibrosus. Journal of the Mechanics and Physics of Solids 54, 1952–1971.

Hiester, E.D., Sacks, M.S., 1998. Optimal bovine pericardial tissue selection sites. Parts I & II. Journal of Biomedical Materials Research 39, 207–221.

Holzapfel, G.A., 2004. Computational Biomechanics of Soft Biological Tissue. In: Encyclopedia of Computational Mechanics. Solids and Structures, vol. 2. Wiley, Chichester, UK, pp. 605–635 (Chapter 18).

Humphrey, J.D., 2003. Continuum biomechanics of soft biological tissues. Proceedings of the Royal Society A – Mathematical Physical And Engineering Sciences 459, 3–46.

Hwang, S., Chang, C., 2000. Determination of elastic constants of materials by vibration testing. Composite Structures 49, 183–190.

Itskov, M., Aksel, N., 2004. A class of orthotropic and transversely isotropic hyperelastic constitutive models based on a poly-convex strain energy function. International Journal of Solids and Structures 41, 3833–3848.

Kang, Y.L., Lin, X.H., Qin, Q.H., 2004. Inverse/genetic method and its application in identification of mechanical properties of interface in composite. Composite Structures 66, 449–458.

Kirkpatrick, S., Gelatt, C.D., Vecchi, M.P., 1983. Optimization by simulated annealing. Science 220, 671–680.

Lamberti, L., 2008. An efficient simulated annealing algorithm for design optimization of truss structures. Computers and Structures 86, 1936–1953.

Lamberti, L., Pappalettere, C., 2007. Weight optimization of skeletal structures with multi-point simulated annealing. Computer Modeling in Engineering and Sciences 18, 183–221.

Limbert, G., Middleton, J., 2004. A transversely isotropic viscohyperelastic material. Application to the modeling of biological soft connective tissues. International Journal of Solids and Structures 41, 4237–4260.

Martins, P.A.L.S., Natal Jorge, R.M., Ferreira, A.J.M., 2006. A comparative study of several material models for prediction of hyperelastic properties: application to silicone-rubber and soft tissues. Strain 42, 135–147.

Massabò, R., Gambarotta, L., 2007. Wrinkling of plane isotropic biological membranes. Journal of Applied Mechanics 74, 550–559.

Mooney, M., 1940. A theory of large elastic deformation. Journal of Applied Physics 11, 582–592.

Ogden, R.W., 1997. Non-linear Elastic Deformations. Dover, Mineola, NY.

Pagnotta, L., 2006. Determining elastic constants of materials with interferometric techniques. Inverse Problems in Science and Engineering 14, 801–818.

Patorski, K., 1993. Handbook of the Moiré Fringe Technique. Elsevier, Amsterdam.

Rao, S.S., 1996. Engineering Optimization. Wiley/Interscience, New York.

Rikards, R., Chate, A., Gailis, G., 2001. Identification of elastic properties of laminates based on experiment design. International Journal of Solids and Structures 38, 5097–5115.

Rivlin, R.S., 1948a. Large elastic deformations of isotropic materials I. Fundamental concepts. Philosophical Transactions of the Royal Society of London A 240, 459–490.

Rivlin, R.S., 1948b. Large elastic deformations of isotropic materials IV. Further developments of the general theory. Philosophical Transactions of the Royal Society of London A 241, 379–397.

Sacks, M.S., 2000. Biaxial mechanical evaluation of planar biological materials. Journal of Elasticity 61, 199–246.

Sacks, M.S., Chuong, C.J., 1998. Orthotropic mechanical properties of chemically treated bovine pericardium. Annals of Biomedical Engineering 26, 892–902.

Sciammarella, C.A., 1972. Use of gratings in strain analysis. Journal of Physics E: Scientific Instruments 5, 833–845.

Sciammarella, C.A., 2003. Overview of optical techniques that measure displacements: Murray lecture. Experimental Mechanics 43, 1–19.

Sciammarella, C.A., Lamberti, L., Sciammarella, F.M., 2005. High accuracy contouring using projection moiré. Optical Engineering 44, 12. Paper No. 015509.

Sciammarella, C.A., Lamberti, L., Boccaccio, A., 2008a. A general model for moiré contouring. Part I: theory. Optical Engineering 47, 15. Paper No. 033605.

Sciammarella, C.A., Lamberti, L., Boccaccio, A., Cosola, E., Posa, D., 2008b. A general model for moiré contouring. Part II: applications. Optical Engineering 47, 15. Paper No. 033606.

Sciammarella, C.A., Lamberti, L., Boccaccio, A., 2008c. High precision contouring with the projection moiré method. Experimental Mechanics (in press).

Sol, H., Hua, H., De Visscher, J., Vantomme, J., De Wilde, W.P., 1997. A mixed numerical/experimental technique for the nondestructive identification of the stiffness properties of fibre reinforced composite materials. NDT-E International 30, 85–91.

Sun, W., Sacks, M.S., 2005. Finite element implementation of a generalized Fung-elastic constitutive model for planar soft tissues. Biomechanics and Modeling in Mechanobiology 4, 190–199.

Van Laarhoven, P.J.M., Aarts, E.H.L., 1987. Simulated Annealing: Theory and Applications. Kluwer Academic Publishers, Dordrecht.

Wineman, A., Wilson, D., Melvin, J.W., 1979. Material identification of soft tissue using membrane inflation. Journal of Biomechanics 12, 841–850.